

Developed liquid film passing a trailing edge: small-scale analysis and the ‘teapot effect’ at large Reynolds numbers

B. Scheichl^{1,2†}, R. I. Bowles³ and G. Pasias³

¹Institute of Fluid Mechanics and Heat Transfer, Faculty of Mechanical Engineering, Technische Universität Wien, Tower BA/E322, Getreidemarkt 9, 1060 Vienna, Austria

²AC2T research GmbH (Austrian Excellence Center for Tribology), Viktor-Kaplan-Straße 2/C, 2700 Wiener Neustadt, Austria

³Department of Mathematics, Faculty of Mathematical & Physical Sciences, University College London (UCL), 25 Gordon Street, London WC1H 0AY, UK

(Received xx; revised xx; accepted xx)

Recently, the authors considered a thin steady developed viscous liquid wall jet passing the sharp trailing edge of a horizontally aligned flat plate under surface tension and the weak action of gravity acting vertically in the asymptotic slender-layer limit (*J. Fluid Mech.* **850**, pp. 924–953, 2018). We revisit the capillarity-driven short-scale viscous–inviscid interaction, on account of the inherent upstream influence, immediately downstream of the edge and scrutinise flow detachment on all smaller scales. We adhere to the assumption of a Froude number so large that choking at the plate edge is insignificant but envisage the variation of the relevant Weber number of $O(1)$. The aspect in the main focus, tackled essentially analytically, is the continuation of the structure of the flow towards scales much smaller than the interactive ones and where it no longer can be treated as slender. As a remarkable phenomenon, this analysis predicts harmonic capillary ripples of Rayleigh type, prevalent on the free surface upstream of the trailing edge. They exhibit an increase of both the wavelength and amplitude as the characteristic Weber number decreases. Finally, the theory clarifies the actual detachment process, unprecedented in the rational theories of flow separation. At this stage, the wetting properties of the fluid and the microscopically wedge-shaped edge, viewed as infinitely thin on the larger scales, come into play. As this geometry typically models the exit of a spout, the predicted wetting of the wedge is related to what in the literature is referred to as the so-called teapot effect.

Key words: boundary layers, thin films, waves/free-surface flows

1. Introduction

We continue to analyse a flow problem of fundamental importance as started in our forerunner study (Scheichl, Bowles & Pasias 2018, hereafter referenced as SBP18).

Let a nominally steady and two-dimensional, developed, slender stream of a Newtonian liquid having uniform properties and at constant flow rate detach from a horizontal, solid, impenetrable, perfectly smooth plate with a trailing edge that is initially considered as

† Email address for correspondence: bernhard.scheichl@tuwien.ac.at

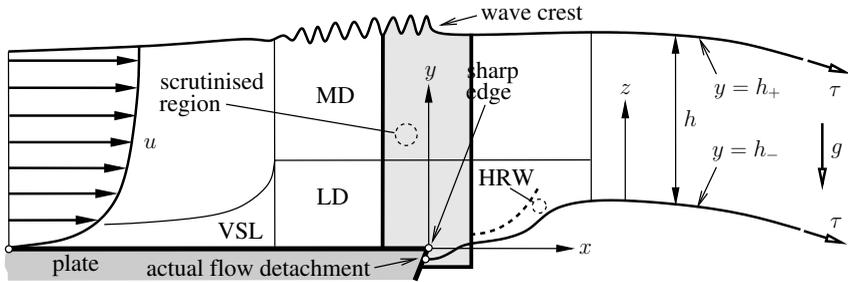


FIGURE 1. Sketch of flow on global, interactive and smaller scales captured by light-shaded region (not to scale, denotations introduced in § 2.1, § 2.3, § 3.2).

abrupt and sharp. Downstream, the flow divides its gaseous environment, fully at rest and under constant pressures, in two parts. Here this picture is relaxed insofar as the upper one still defines the zero pressure level but we allow for a non-zero, constant support pressure prescribed at the downside of the detached layer. The body and interface forces crucially at play are the constant gravitational acceleration acting vertically towards the wetted side of that plate and surface tension. Based on the principle of least degeneration, our rigorous theoretical description of the detaching thin film under the assumption of very supercritical flow adopts a specific distinguished limit where the relevant Reynolds and Froude numbers are taken as asymptotically large but the corresponding Weber number as of $O(1)$. Hence, the exciting details accompanying the detachment process are governed by a strong viscous–inviscid, shortened-scale interaction at the outset of our present study.

1.1. Studied phenomena and open questions

Our current concern is with the analytical/numerical challenges arising in the analysis of the free jet with particular emphasis placed on the description of its detachment at the abrupt plate edge on the smallest scales and the freely interacting flow immediately downstream of the trailing edge. As a key observation in SBP18, this is strongly reminiscent of its detachment and therefore the no-slip condition satisfied further upstream. Since the interaction mechanism is not yet capable of smoothing the flow quantities at the sharp edge, coping with this demand addresses the flow on still smaller and down to the smallest scales discernable and eventually the wetting properties of the plate as well as the geometry forming its edge. The remarkable ramifications of such an analysis are threefold:

- (i) As a first cornerstone, it reveals the existence of (stationary) undamped capillary Rayleigh modes upstream of its break-away from the plate.
- (ii) The stratification of the flow given the largeness of the Reynolds number prevents its separation upstream of the trailing edge, which confirms the initially made assumption of detachment “at the edge” considered on larger scales.
- (iii) As a second highlight, the implied wetting of the edge suggests an unprecedented rational explanation of the so-called teapot effect observed in a high-momentum wall jet when a convex corner provides – in a most simple but nevertheless sufficiently complex manner – the non-degenerate geometry modelling the plate edge.

Subsequently, we refer to the sketch in figure 1 throughout, illustrating the different flow regions considered when viewed on the global scale.

The paper has the following structure. (So as not to distract attention away from the

main arguments, some technical points as well as interesting side aspects are detailed in appendices.)

§ 1.2: As a start, we critically review the prevailing and rather phenomenological view on the teapot effect and its previous modelling.

§ 2: We then pose the problem based on first principles in full. Considering our basic scaling arguments (§ 2.1) demonstrates their applicability to the teapot phenomenon in typical settings (§ 2.2). This justifies the use of asymptotic analysis as the means of choice to study the flow, initiated by completing the formulation of the interaction problem, originally posed in SBP18. It then governs the continuation of the freely interacting jet downstream of the edge in a rigorous manner as long as the value of the appropriately rescaled Weber number does not fall below a certain threshold, so avoiding the onset of nonlinear stationary capillary waves even on the wall jet (§ 2.3).

§ 3: A thorough investigation of the multi-structured small-scale flow locally superseding the two-tiered interactive structure shows that this gives way to two nested square Euler regions. The exterior one, extending vertically across most of the layer, is the source of phenomenon (i) above on the top free surface.

§ 4: This essentially inviscid description of flow detachment paves the way for to a full Navier–Stokes (NS) regime detected on even smaller streamwise and vertical scales. Its study boils down to the implication (ii) above. As a pivotal finding, achievement (iii), we also identify one or two interlaced Stokes regions resolving the smallest scales and the actual wedge-type resolution of the plate end, until now seen as infinitely thin. Consequently, it is this flow regime where the break-away of the film, interacting with the larger-scale flow through the NS region, is finally controlled by both the edge geometry and the static wetting angle. An awareness of the close relationship of this situation to the teapot effect is then gained.

§ 5: Surveying the current results for our ongoing research and the inclusion of such effects as unsteadiness and the aforementioned capillary undulations complete the study.

All our numerical calculations took consequently and efficiently advantage of the widely-used, proprietary programming language and numerical-computing environment *MATLAB* (2020), supplemented with *The NAG Toolbox* (2020). In particular, the computations benefit from its convenient handling of complex data and the, in principle, built-in arbitrary accuracy and precision.

1.2. The teapot effect: a digression

The frequently observed, at a first glance spontaneous (and often undesired) tendency of a liquid pouring from a spout to instead stick to its underside was originally reported by Reiner (1956, also see the references therein): see figure 2(a). More precisely, he coined the notion “teapot effect” for pouring liquid along a rigid convex wall with a marked corner and adjoining to another (even liquid) fluid. He untangled the riddle of its occurrence experimentally: his observations ruled out the hitherto widely held belief that the wetting properties in terms of short-range inter-molecular adhesion forces, promoted by wetting agents, are its essential cause. However, his various experiments demonstrated that “adhesion” as the reaction force on the fluid flowing over a solid phase as well as surface tension at its common interface with the surrounding fluid play a decisive role. A most recent survey of the various treatment of this scenario presented by Jambon-Puillet *et al.* (2019, see the references therein) spans the rigorous approach within the framework of classical fluid mechanics, outlined below, to the nowadays more common but less stringent approach. This seeks the pivotal cause for fluid sticking rather than being poured in the hydrophilic tendency of the liquid/wall pairing. The latter authors provide new insight by coupling these ideas with classical argument resorting to the first

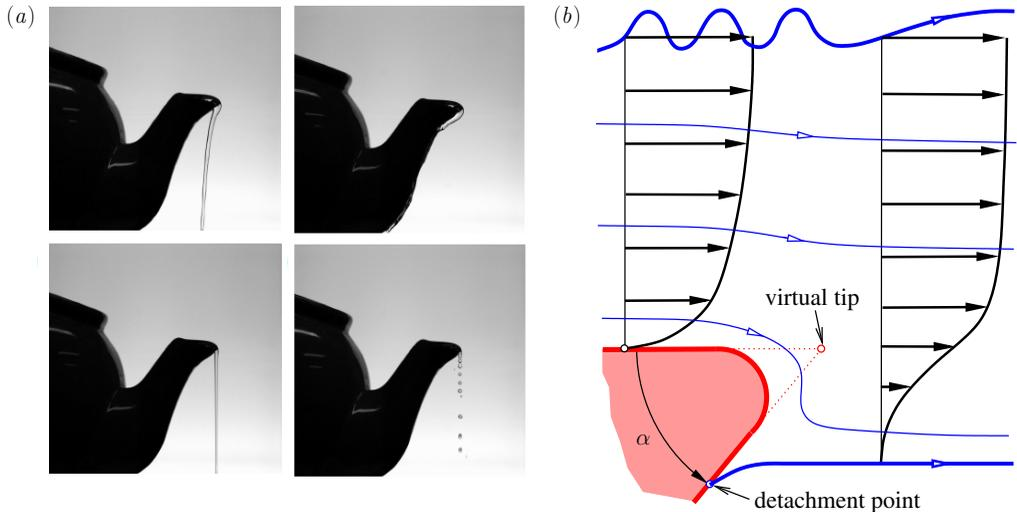


FIGURE 2. (a) Different realisations of the teapot effect for a low-momentum jet typically strongly subject to gravity, described in and reprinted with permission from [Duez *et al.* \(2010\)](#) (© by the American Physical Society); (b) its current abstraction for a horizontal high-momentum jet passing a rounded wedge of angle α , detailing the flow around the trailing edge in figure 1, typical no slip on the plate and free slip along the free streamlines, blue: free and internal streamlines and detachment point, red: plate and original (virtual) tip in figure 1.

principles of continuum mechanics. Notably, [Duez *et al.* \(2010\)](#) flag up a preminent reduction of the effect via the application of superhydrophobic substrates.

We advocate continuum mechanics for providing a satisfactory, rational unravelling of the effect. In agreement with the above early observations, we interpret it as a subtle interplay of inertia, capillarity and gravity. This is crucially tied in with the breakdown of viscous–inviscid interaction and thus the slender-layer approximation on larger scales due to assumed largeness of the globally defined Reynolds number of the oncoming attached flow. The significance of capillarity and inertia lies also in the proper adjustment of the latter. Our asymptotic theory proposes a fully rational account of the onset of this phenomenon in the realistic situation of a developed incident flow. As a specific ingredient, the trailing edge is replaced by a kink, i.e. a wedge formed by an acute cut-back angle or lip: this “attracts” the wall jet such that it clings to it before the liquid sheet breaks away from it as a whole away from its underside. This phenomenon of free rather than forced gross separation from a convex rigid surface, consequently referred to as the teapot effect from here onwards, does not yet benefit from a satisfactorily rigorous and complete description.

This effect has experienced a first self-consistent clarification under the quite restrictive assumption of irrotational flow of a weightless ideal fluid past a horizontal plate terminated by the aforementioned lip: remaining firmly attached both with the neglect of gravity ([Keller 1957](#)) and under gravity ([Vanden-Broeck & Keller 1986](#)); detaching grossly from the underside at zero gravity ([Vanden-Broeck & Keller 1989](#)).

Rather little is known when it comes to the rigorous inclusion of viscosity in this flow picture. The incident flow was taken as developed in all relevant studies, on an account to model the real situation. At least, the passage of a layer over an asymptotically small convex wall corner (and in related situations) considered by [Gajjar \(1987\)](#) (and the refined numerical results by [Yapalparvi 2012](#)) bears some relevance. Specifically, there the unperturbed oncoming flow is fully developed as already inclined towards gravity,

and viscous–inviscid interaction of the double-layer structure in the high-Reynolds-number limit adopted here negotiates the accordingly slender obstacle. However, the counteracting surface tension in the characteristic combined hypersonic- and wall-jet-type interaction law (cf. Bowles & Smith 1992) is ignored in the analysis although mentioned. Although the interactive flow considered by Gajjar (1987) is *assumed* to remain grossly attached, it is interesting by all means that the numerical solutions predict a closed separation bubble beyond the mild wedge for both sufficiently large turning angles and Froude numbers.

A seminal reference for the teapot effect in a realistic, i.e. developed, flow is the numerical and partially analytical investigation of the full NS problem by Kistler & Scriven (1994). They unambiguously highlighted its viscous and capillary, i.e. hydrodynamic, nature as underpinned by experimental evidence. This prompted them to conclude that “the teapot effect is more than merely an issue of wetting”. Most remarkably, they pointed out how the restrictions of the microscopic wedge-type geometry of what is on larger scales viewed as an “infinitely sharp” edge implies a contact-angle hysteresis, associated with non-unique flow states, but the point of flow detachment assumes the apex of the wedge when the jet Reynolds number, i.e. the momentum it carries, becomes sufficiently large. The present asymptotic analysis corroborates this finding, where we deal with a horizontal oncoming flow past a wedge originally represented by a cut-back angle α ($0 < \alpha < \pi$), using equal horizontal and vertical scales. However, here the wedge is no longer necessarily sharp as we allow for its tip being realistically rounded: see the sketch in figure 2(b).

2. Statement of the extended problem

It proves expedient to first reappraise the fundamental assumptions and the problem in full before revisiting the interactive limit.

2.1. Non-dimensional groups and governing equations

The problem formulation adopts the following central ingredients where we endow dimensional quantities with tildes. The slender layer of density $\tilde{\rho}$ and kinematic viscosity $\tilde{\nu}$ and experiencing a tensile surface stress $\tilde{\tau}$ and gravitational acceleration \tilde{g} carries a volume flow rate per unit depth \tilde{Q} . It adjusts to a developed state over some sufficiently large distance \tilde{L} , serving as the basic length scale and measured along the plate from its trailing edge in the upstream direction. Simultaneously, \tilde{L} is required to be so short that the vertical layer height has not grown sufficiently to allow for a significant impact of the hydrostatic pressure on streamwise convection. Then a layer height $\tilde{H} = \tilde{L}\tilde{\nu}/\tilde{Q}$ and flow speed $\tilde{U} = \tilde{Q}^2/(\tilde{\nu}\tilde{L})$ representative of this near-supercritical film follow from conservation of the flow rate and the streamwise momentum, here expressed by the balance between convection and the shear stress gradient, respectively

$$\tilde{Q} = \tilde{U}\tilde{H}, \quad \tilde{U}^2/\tilde{L} = \tilde{\nu}\tilde{U}/\tilde{H}^2. \quad (2.1)$$

In many applications, height and, accordingly, speed of the layer have respectively increased and decreased so markedly over \tilde{L} that it has almost attained its well-known perfectly supercritical, *fully* developed or self-preserving state discovered by Watson (1964): for related discussions see Bowles & Smith (1992), Higuera (1994) and, in the context of an axisymmetric and rotatory layer, Scheichl & Kluwick (2019) generated by vertical jet impingement.

The flow is then controlled by the slenderness parameter or reciprocal Reynolds number

ϵ and corresponding reciprocal Froude and Weber numbers g and τ :

$$\epsilon := \tilde{H}/\tilde{L} = \tilde{\nu}/(\tilde{U}\tilde{H}) \ll 1, \quad g := \tilde{g}\tilde{H}/\tilde{U}^2 = O(\epsilon^{4/7}), \quad \tau := \tilde{\tau}/(\tilde{\rho}\tilde{U}^2\tilde{H}) = O(1). \quad (2.2a)$$

As for the distinguished limit involving g , locally strong viscous–inviscid interaction describes the abrupt transformation of the wall-bounded jet towards the free liquid jet in a least-degenerate, self-consistent and sufficiently smooth manner. We remark that the conventionally defined capillary number

$$Ca := \tilde{\rho}\tilde{\nu}\tilde{U}/\tilde{\tau} = \epsilon/\tau \ll 1 \quad (2.2b)$$

or the alternative Ohnesorge number, here $\epsilon/\sqrt{\tau} \ll 1$, provide different albeit less preferable introductions of the surface tension for a layer of small slenderness measured by ϵ : since the streamline curvature scales with $\tilde{H}/\tilde{L}^2 = \epsilon^2/\tilde{H}$, the ratio of the viscous (deviatoric) stress normal to a free surface and scaling with $\tilde{\rho}\tilde{\nu}\tilde{U}/\tilde{L} = \tilde{\rho}\tilde{U}^2\epsilon^2$ to the capillary hoop pressure measured by $\tilde{\tau}\tilde{H}/\tilde{L}^2 = \tau\epsilon^2\tilde{\rho}\tilde{U}^2$ is expressed by the augmented capillary number $Ca/\epsilon = 1/\tau = O(1)$, taking into account the aspect ratio of the flow. This indicates that in the limit provided by (2.2a) the surface jump of the total normal stress is fully retained in the dynamic boundary conditions (BCs) below.

We introduce Cartesian coordinates x and y pointing respectively horizontally from the trailing edge and vertically towards the flow, the streamfunction ψ and the pressure p , non-dimensional with \tilde{L} , \tilde{H} , \tilde{Q} and $\tilde{\rho}\tilde{U}^2$ respectively. Then $u := \psi_y$ is the horizontal and $v := -\epsilon\psi_x$ the vertical flow component made dimensionless with \tilde{U} . These $O(1)$ -quantities satisfy the NS equations in the form

$$\psi_y\psi_{yx} - \psi_x\psi_{yy} = -p_x + (\epsilon^2\partial_{xx} + \partial_{yy})\psi_y, \quad (2.3a)$$

$$\epsilon^2(\psi_x\psi_{yx} - \psi_y\psi_{xx}) = -p_y - (\epsilon^2\partial_{xx} + \partial_{yy})(\epsilon^2\psi_x) - g. \quad (2.3b)$$

Here and hereafter, derivatives are unambiguously indicated by subscripts; the subscripts $-$ and $+$ indicate the evaluation along the lower- and the uppermost free streamline respectively. Accordingly, $y = h_-(x)$ ($\equiv 0$ for $x \leq 0$) and $y = h_+(x)$ denote their positions, hence $h(x) := h_+ - h_-$ the vertical film thickness and p_{\pm} the given pressure levels along the free streamlines. Adopting the Heaviside step function θ then gives the kinematic boundary conditions including the conventional requirements of no slip at and no penetration of the plate as follows.

$$y = h_-(x): \quad \psi = \psi_y\theta(-x) = 0, \quad y = h_+(x): \quad \psi = 1. \quad (2.3c)$$

The dynamic BCs express vanishing tangential stresses and total normal stresses equal to the capillary pressure jumps on the free surfaces of curvatures $\varkappa_{\pm}(x)$ and subject to the Young–Laplace equilibrium. Therefore, at

$$y = h_-(x) \text{ if } x > 0, \quad y = h_+(x):$$

$$(1 - \epsilon^2 h_{\pm}^{\prime 2})(\psi_{yy} - \epsilon^2\psi_{xx}) - 4\epsilon^2 h_{\pm}^{\prime}\psi_{yx} = 0, \quad (2.3d)$$

$$\left. \begin{aligned} 2\epsilon^2[\psi_{yx}(1 - \epsilon^2 h_{\pm}^{\prime 2}) + h_{\pm}^{\prime}(\psi_{yy} - \epsilon^2\psi_{xx})]/(1 + \epsilon^2 h_{\pm}^{\prime 2}) + p - p_{\pm} &= \tau\varkappa_{\pm}, \\ p_{\pm} = 0, \quad \varkappa_{\pm} &= \mp\epsilon^2 h_{\pm}^{\prime\prime}/(1 + \epsilon^2 h_{\pm}^{\prime 2})^{3/2}. \end{aligned} \right\} \quad (2.3e)$$

This completes the problem (2.3) as proper up- and downstream conditions will be condensed into requirements of continuity holding at the trailing edge $x = 0$.

2.2. Order of magnitudes and their physical relevance

Even though left unspecified here, a horizontal nozzle or impingement of a vertical jet represent the most viable sources generating a flow configuration of engineering

| | | | | | | | |
|-----------------------------------|------------------------------------|-----------------------|---------------------------------|---------------------|-------------------------|------------------|-------------------|
| $\bar{\rho}$ (kg/m ³) | $\tilde{\nu}$ (mm ² /s) | $\tilde{\tau}$ (mN/m) | \tilde{g} (m/s ²) | \tilde{Q} (l/min) | \tilde{L} (mm) | \tilde{H} (mm) | \tilde{U} (m/s) |
| 998.20 | 1.00 | 72.75 | 9.81 | $\gtrsim 6$ | $\approx 50\text{--}60$ | ≈ 1 | > 0.1 |

TABLE 1. Typical input data (water at standard conditions).

| | | | | |
|------------|-----|--------------|-------------------|---------------|
| ϵ | g | τ | Ca | Ca/ϵ |
| 0.01–0.02 | 0.1 | $\lesssim 7$ | $\gtrsim 0.00137$ | 0.0686–0.137 |

TABLE 2. Typical key parameters resulting from table 1.

concern. This then unequivocally refers to variety of physical scenarios. However, one might question the validity of the order-of-magnitude stipulations made in (2.2a) in view of a realistic, conceivable situation of industrial importance or even observations in daily life (as a flow generated by wielding a teapot, for instance). Such a setting is characterised by feasible geometrical and flow conditions and an aqueous, viscous fluid under the action of gravity and surface tension. Indeed, the chosen largeness of the Froude number at a moderate Weber number deserves some comment. The following arguments yielding the values of the non-dimensional groups in (2.2), see the tables 1 and 2, refer to a jet of pure water under standard conditions.

With $\tilde{\tau} \lesssim 100$ mN/m throughout (water as a polar liquid, and of potential interest, has a comparatively high surface tension), an adequately small Bond number $g/\tau = \tilde{g}\tilde{\rho}\tilde{H}^2/\tilde{\tau}$ (neglect of gravity over surface tension) is, however, definitely not smaller than $10^5 \text{ m}^{-2} \times \tilde{H}^2$. This requires $\tilde{H} \approx 1$ mm; for much smaller film heights, effects originating in technically unavoidable geometric imperfections of the plate surface might no longer be negligible (but worthy of study). Likewise, $g \ll 1$ (neglect of gravity over inertia) is achieved if $\tilde{U} \gg 0.1$ m/s. Given their rather narrow range of physically acceptable values and prediction of an extremely thin and fast film, these estimates have admittedly to be adopted with some caution. As an essential finding, the Reynolds number ϵ^{-1} proves indeed large but not to the extent that laminar–turbulent transition becomes an issue. However, the accompanying rather large value of τ gives reassurance to these doubts as it points to a numerically rather high sensitivity of the key parameters to slight variations of the input data. Also, $\epsilon = O(g^{7/4})$ for e.g. $g = 0.1$ implies a reference or effective plate length \tilde{L} of about 5 to 6 cm, which seems sensible, and $\epsilon \approx 0.018$. We check the reliability of the last estimate on the basis of the second relationship defining ϵ in (2.2a): the above estimate for \tilde{U} predicts values for ϵ barely smaller than 0.01. Given the potential variety of the input data, we achieve a satisfactorily good agreement. Our prerequisites, condensed in (2.2a), can then be considered as self-consistent.

Most critically, the validity and sensitiveness of the scalings originate in a sufficiently small typical film height \tilde{H} rather than in the values of the remaining physical parameters. Nonetheless, the subsequent asymptotic analysis of (2.3) in the distinguished limits provided by (2.2a) remains valuable even if the underlying order-of-magnitude estimates should be interpreted with a greater flexibility. In particular, the actual value of τ is taken as definitely smaller than its upper bound stated in table 2 from here onwards.

2.3. Free interaction downstream of the trailing edge

The governing equations (2.3) and (2.2a) immediately give rise to a regular expansion valid for the flow above the plate on the original large streamwise scale, i.e. for $1 + x = O(1)$, $0 > x = O(1)$:

$$[\psi, h, p/g] \sim [\psi^0(x, y), h^0(x), h^0(x) - y] + O(g), \quad [\psi^0, h^0] \sim [\psi_0(y), h_0] \quad (x \rightarrow 0-). \quad (2.4)$$

In the leading order of this non-interactive limit, the classical parabolic shallow-water approximation of (2.3) is recovered, predicting a pressure-free base flow described by ψ^0 and h^0 . These quantities approach regularly some values ψ_0 and h_0 at the trailing edge. The higher-order contributions in (2.4) control the modification by the hydrostatic pressure distributions and non-parallel-flow effects, the latter predominantly due to streamline curvature, capillary action and the viscous normal stresses $\pm \epsilon^2 \psi_{yx}$, in the following iterative manner. At each level of improvement, an obtained approximation for ψ feeds into (2.3b) subject to (2.3e). The so determined pressure correction then forces a problem that emerges from expanding (2.3a) subject to (2.3c) and (2.3d) and governs a further correction for ψ , and so on.

Following SBP18, this hierarchy is singularly perturbed by weak irregular disturbances exhibiting exponential growth over a short streamwise scale measured by $\epsilon^{6/7}$. Thus, they are active in a viscous sublayer (VSL) adjacent to the plate. Hence subject to free viscous–inviscid interaction governed by streamline curvature, not accounted for in the classical shallow-water limit, they describe the intrinsic upstream influence in the film caused by both gravity and capillarity. Finally, the growth of these two effects renders the above hierarchy invalid around the trailing edge where $x = O(\epsilon^{6/7})$ and they provoke a locally strong interaction over that scale in the limits (2.2a). This typically involves a nonlinear distortion of the strongly viscosity-affected slow flow in the lower deck (LD), here originating in the aforementioned sublayer, adjacent to the lowermost streamline where $y = O(\epsilon^{2/7})$. The latter exerts a linear response in the main deck (MD) that comprises the bulk of the layer, confined by the upper free streamline.

The background flow enters the interactive scalings in leading order solely via two quantities condensing its upstream history: the momentum flux J over the trailing edge and the shear stress λ exerted on it,

$$J := \int_0^{h_0} \psi_0'^2(y) dy, \quad \lambda := \psi_0''(0) \quad \text{as} \quad \psi_0 \sim \frac{\lambda y^2}{2} + \frac{\lambda \omega y^5}{60} + O(y^8) \quad (y \rightarrow 0). \quad (2.5)$$

The coefficient ω is only relevant in the small-scale analysis. We also note (2.3c) and the free-slip condition resulting from (2.3d):

$$\psi_0(h_0) = 1, \quad \psi_0''(h_0) = 0. \quad (2.6)$$

Usually, \tilde{H} as in table 1 is definitely larger than the height of the film immediately downstream of its origin (as given by jet impingement) and where the flow starts to become developed. This prompts one to consider the base flow as having already assumed Watson’s (1964) self-similar one and to neglect the small deviations from this due to the flow history, as in SBP18 and without any substantial loss of generality. In this idealisation, $h^0 = \pi(x - x_v)/\sqrt{3}$ provided some $x = x_v < 0$ indicates the virtual origin of the fully developed flow and ψ^0 is a universal function of y/h^0 . At $x = 0$, ψ_0 then satisfies

$$\psi_0'^2 = x_v \psi_0''' \quad (2.7)$$

and has an exact representation given by Scheichl & Kluwick (2019). With u_0^+ reasonably

abbreviating $\psi'_0(h_0)$ from here on, this implies the important results

$$\frac{h_0}{|x_v|} = \frac{\pi}{\sqrt{3}} \simeq 1.8138, \quad x_v^2 \lambda = |x_v| J = \frac{[|x_v| u_0^+]^{3/2}}{\sqrt{3/2}} = \frac{[\Gamma(\frac{1}{3})/\Gamma(\frac{5}{6})]^3}{2\sqrt{3}\pi^{3/2}} \simeq 0.69301. \quad (2.8)$$

The interaction process itself is parametrised by suitably redefined reciprocal Froude and Weber numbers G and T and the rescaled support pressure P_- , all of $O(1)$. Specifically, T is formed with the local momentum flux and thus measuring the influence of capillarity relative to fluid inertia. We thus introduce

$$(G, P_-) := (gh_0, p_-)/(M^2 \lambda^6 \epsilon^4)^{1/7}, \quad T := \tau/J, \quad M := |T - 1|J = |\tau - J|. \quad (2.9)$$

The above prepositions enable us to reconsider the interaction problem, at first under the assumption of T being not too close to unity. For the details of its numerical treatment by specifying ψ_0 as Watson’s flow profile and marching downstream we refer to SBP18.

In table 1, the first six parameters serve as input quantities defining \tilde{H} and \tilde{U} via (2.1). For a given flow, we note the invariance of (2.1) and thus of ϵ , ψ , (2.3) and G , T , P_- against the affine transformation

$$(\tilde{L}, \tilde{H}, \tilde{U}, x, y, h_{\pm}, p, g, \tau, J, \lambda) \mapsto \left(a\tilde{L}, a\tilde{H}, \frac{\tilde{U}}{a}, \frac{x}{a}, \frac{y}{a}, \frac{h_{\pm}}{a}, a^2 p, a^3 g, a\tau, aJ, a^2 \lambda \right) \quad (2.10)$$

with an arbitrary scaling factor $a > 0$. It confirms the independence on \tilde{H} of the canonical formulation of the interaction problem below and thus on the specific choice of the streamwise length scale \tilde{L} (for a sufficiently small $\epsilon = \tilde{H}/\tilde{L}$). In particular, its solution downstream of the edge does not depend on the scaling of the attached flow and, specifically, the position of the aforementioned virtual origin. For any subsequent numerical evaluation involving ψ_0 and h_0 , however, we not only assume the flow as being fully developed but also adopt the natural standardisation $x_v = -1$ from here on, i.e. specify \tilde{L} as the development length.

2.3.1. Main deck

Since the MD describes a predominantly inviscid flow in the long-wave limit, the central local expansion reads

$$\begin{aligned} [\psi, h, h_-, h_+] &\sim [\psi_0(z), h_0, 0, h_0] + \epsilon^{2/7} m [A(X) \psi'_0(z), -A(X), H_-(X), H_+(X)] \\ &\quad + O(\epsilon^{4/7}), \quad H_+ := H_- - A, \quad m := (M/\lambda^4)^{1/7}, \quad z := y - h_-(x), \end{aligned} \quad (2.11)$$

and p is of $O(\epsilon^{4/7})$. The local streamwise variable $X = O(1)$ is defined in (2.13) below. The expansion (2.11) induces the following hierarchy of equations resulting from the Euler operator in (2.3a,b). The dominant viscous displacement exerted by the LD, $-A(X)$, generates typically the dominant perturbation of ψ about ψ_0 in terms of the pressure-free eigensolution of the linearised streamwise momentum equation (2.3a), where we have conveniently introduced the Prandtl transposition. Entering (2.3b), this $O(\epsilon^{2/7})$ -contribution to ψ governs streamline curvature and, by virtue of integration with respect to y , the convective portion supplementing the hydrostatic portion of $p = O(\epsilon^{4/7})$. The disturbances described so far account for the role of the MD for the interactive mechanism. The $O(\epsilon^{4/7})$ -contributions to p and to ψ , the latter induced subsequently by the streamwise pressure gradient, are specified in SBP18.

2.3.2. Lower deck

In the LD, the expansion

$$[\psi, p]/\epsilon^{4/7} \sim [(M^2/\lambda)^{1/7} \Psi(X, Z), (M^2 \lambda^6)^{1/7} P(X)] + O(\epsilon^{6/7}) \quad (2.12)$$

employs the stretched coordinates

$$X := xl/\epsilon^{6/7}, \quad (Y, Z) := (y, z)/(m\epsilon^{2/7}), \quad l := (\lambda^5/M^3)^{1/7}. \quad (2.13)$$

To describe the up- and downstream of the plate edge, Z is used preferably over Y in the slender LD. In turn, (2.3a,b) reduce locally to the boundary layer equation

$$\Psi_Z \Psi_{ZX} - \Psi_X \Psi_{ZZ} = -P' + \Psi_{ZZZ}, \quad (2.14a)$$

and (2.3c,d) to the mixed BCs expressing the downstream passage from no- to free slip along

$$Z = 0: \quad \Psi = \Psi_Z \theta(-X) = \Psi_{ZZ} \theta(X) = 0. \quad (2.14b)$$

To match (2.12) and (2.11) subject to (2.5), we require for

$$Z \rightarrow \infty: \quad \Psi \sim [Z + A(X)]^2/2 [+P(X) + \text{TST}]. \quad (2.14c)$$

The bracketed contribution herein is a consequence of (2.14a); TST means transcendently small terms.

Relating the displacement function A to P closes the interactive feedback loop and the weakly elliptic free-interaction problem. For $X < 0$, that relationship is given by the jet-type interaction law $P - G = S(A'' - H_-'')$, typically provoked by the streamline curvature in the MD and the (counteracting) capillary pressure jump across the uppermost streamline (as introduced by Smith 1977; Smith & Duck 1977 and, for an unconfined jet passing an abrupt edge, Smith 1978); for $X > 0$, one eliminates H_- from the interaction law via the representation of P in terms of the pressure jump across the lowermost streamline to which (2.3e) reduces:

$$\Delta P \theta(X) = TH_-''/|T - 1|, \quad \Delta P := P - P_-. \quad (2.14d)$$

(in SBP18 only the case $P_- = 0$ was considered). We thus arrive at the P/A law in the form

$$\Delta P = C(T)(G + SA'' - P_-), \quad S := \text{sgn}(T - 1), \quad (2.14e)$$

$$C(T) := \begin{cases} 1 & (X \leq 0), \\ T/(2T - 1) & (X > 0). \end{cases} \quad (2.14f)$$

We furthermore introduce $D(T) = 1 - C(T)$. The upstream case is included in this interaction law for the sake of completeness and clarity. Downstream of the edge, it accounts for a subtle interplay of capillarity with inertia; the functions C and D plotted in figure 3 are consulted tacitly from here on. The pole of C points to an interesting local increase of the capillary action for $T \sim 1/2$. The passage of T over this threshold is associated with a breakdown of the existing flow description for the free jet. It requires the introduction of even shorter scales and can be interpreted as choking of a capillary wave. A second critical value $T = 1$ ($S = 0$) describes the cancelling of the counteracting effects of streamline curvature and capillarity on the transverse momentum transfer. Both are subsumed by A'' and are thus resorted to the viscous forcing of the LD. The absence of this effect gives condensed interaction, where H_- remains unspecified according to (2.14d), unless A grows significantly to allow for a regularisation. Both exceptional situations are skated over below (§ 2.3.3) and still subject of ongoing investigations.

The rescaled shear stress exerted at the plate, $A(X) := \Psi_{ZZ}(X, 0)$, plays a crucial role for the (unambiguous) formulation of the initial conditions (ICs) imposed at the plate edge $X = 0$ by SBP18 for the detached flow, controlling its upstream influence on the plate-bounded flow in a unique manner. The detailed rationale underlying these deserves to be clarified in terms of the follows steps.

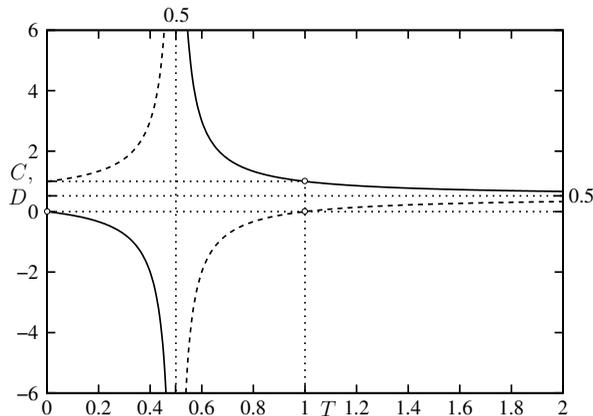


FIGURE 3. $C(T)$ (solid) and $D(T)$ (dashed) by (2.14f) ($X > 0$) with their asymptote and poles (dotted), fixed point and zeros (circles).

(I) The two original demands on the interaction mechanism were the simultaneous continuous approach of the overall pressure jump across the layer towards $-P_-$ and of Λ towards zero in the limit $X \rightarrow 0-$, but only the first of these typical edge conditions can be met;

(II) if

$$\epsilon^{12/7} \ll T < 1 \quad (S = -1, T \neq 1/2), \quad (2.14g)$$

the conditions the flow has to meet at the edge can then be formulated without resorting to the analysis of smaller regions enclosing the edge;

(III) then a least-degenerate flow description that allows for a smooth gradual transition from attachment to detachment of the flow quantities on smaller streamwise scales requires continuity of Ψ and A' above the edge.

In turn, the three ICs required to continue marching of Ψ and P , satisfying the with respect to X first- and second-order equations (2.14a) and (2.14e), over the edge

$$\Psi_0 := \Psi(0+, Z) = \Psi(0-, Z) \quad (Z > 0), \quad T[A'(0+) - A'(0-)] = 0, \quad P(0) = P_- \quad (2.14h)$$

complete the interaction problem (2.14) for the free jet. Here the flow profile at detachment $\Psi(0-, Z)$ and $A'(0-)$ are taken as obtained by the preceding sweep of numerical marching towards the edge. It is stressed that Ψ , P behave regularly as $X \rightarrow 0-$. Moreover, these quantities are continuous across the edge except for the shear stress Ψ_{ZZ} on $Z = 0$, owing to (2.14b).

We also recall the behaviour inferred from (2.14a,b) for

$$Z \rightarrow 0: \quad \Psi \sim \begin{cases} \Lambda(X)Z^2/2 + P'(X)Z^3/6 + O(Z^5) & (X \leq 0), \\ U_s(X)Z + [P' + U_s U_s'](X)Z^3/6 + O(Z^5) & (X > 0). \end{cases} \quad (2.15)$$

Hence, the finite slip emerging along the lower free streamline, U_s , supersedes the finite plate stress Λ upstream of the edge. We note that (2.15) first implies

$$\Psi_0 \sim \Lambda_0 Z^2/2 + P'(0-)Z^3/6 + O(Z^5) \quad (Z \rightarrow 0), \quad \Lambda_0(G, T) := \Lambda(0-). \quad (2.16)$$

The apparent non-uniformity of (2.16) for $X = 0+$ is the topic of §3.2 below. The parameters G and P_- , representing the freely chosen support pressure, enter the solution of the interaction problem only via (2.14h), i.e. G in terms of the imposed momentum flux, and subsequent integration of $P'(X)$ found in the course of the marching procedure. The decoupled calculation of H_- is finally provided by (2.14d). Eliminating P with the

aid of (2.14e) gives the alternative relation

$$H_-(X) = D(T)[A(X) - A(0-) - A'(0-)X + (G - P_-)SX^2/2], \quad (2.17)$$

i.e. $H_-(0) = H'_-(0) = 0$. Evidently, the support pressure behaves as a body force counteracting gravity.

2.3.3. Some important aspects

To achieve the last requirement in (2.14h), the interaction is initiated in the limit $X \rightarrow -\infty$ by a controlled branching from the oncoming base flow, here maintained as the trivial solution $\Psi \equiv Z$ for $X \leq 0$ if $G = P_- \geq 0$. Hence, the case $G > P_-$ requires branching of expansive type as scrutinised by SBP18 (where $P_- = 0$ throughout) and the opposite one $0 \leq G < P_-$ compressive branching (unconsidered so far). However, since $A''(X)$ is the streamline curvature in the interactive limit, it becomes evident from (2.14e) that the interactive feedback loop triggers stationary capillary waves iff $SC > 0$. Here this implies $0 < T < 1/2$ or $T > 1$; see the preceding studies by Bowles & Smith (1992) and SBP18 and the preliminary presentation of these undulations by Scheichl, Bowles & Pasias (2019).

For the following instructive analogy to linear, planar (unconditionally stable) Rayleigh–Plateau modes perturbing a planar, uniform jet having constant speed in the x -direction and two free surfaces $y = 0$ and $y = h_0$ we refer the reader to Drazin & Reid (2004, p. 30 and §5). Let k denote their wavenumber, non-dimensional with \tilde{H} , and c the ratio of their phase speed relative to the unperturbed jet speed. Using the definition of J , we obtain the classical anomalous dispersion relation in the form

$$(c - 1)^2 = Tk \times \begin{cases} \coth(k/2) & \text{(skew-symmetric modes),} \\ \tanh(k/2) & \text{(symmetric modes).} \end{cases} \quad (2.18)$$

Here the symmetry refers to the u -perturbation with respect to the centreline $y = h_0/2$. Hence, the antisymmetric modes give the picture of a sinusoidally meandering jet as $h_+ \sim h_0 + h_-$ and h_- are in phase. On the contrary, they are in antiphase as $h_+ \sim h_0 - h_-$ for the symmetric modes, producing a “varicose” or symmetrically looking jet. The latter modes appear visually as the classical axisymmetric modes on a circular jet. There exists a single stationary, choked mode ($c = 0$) for each value of T in the symmetric case but but only for $T < 1/2$ in the antisymmetric one, where indeed $T \rightarrow 1/2-$ in the long-wave limit $k \rightarrow 0$, resembling the interactive limit. Moreover, our first numerical solutions of (2.14) predict a sinusoidal modulation only of the detached jet if $0 < T < 1/2$ and of varicose kind in the yet poorly-understood case $T > 1$, where the onset of the waviness of the upper free surface approaches the edge from upstream as T tends to 1 from above (see SBP18). These results allow for the subsequent interpretation. The undulations for the first T -range represent a nonlinear, viscosity-affected variation of their classical counterpart, also strongly impacted by the background vorticity or the reduced fluid velocity at the lower interface. Like the classical ones, these vanish only for vanishing capillarity. For T sufficiently exceeding 1, the predominance of capillarity over both vorticity and the symmetry-breaking displacement effect implements a nonlinear modification of steady varicose modes. This analogy becomes evident from inspection of (2.11), (2.17) and figure 3: for sufficiently large $|A|$, we have $H_+ \sim (D - 1)H_-$; thus $\text{sgn}(H_+) = \text{sgn}(H_-)$ for $T < 1/2$ and $\text{sgn}(H_+) = -\text{sgn}(H_-)$ for $T > 1/2$, where the symmetry of the varicose waves downstream of the plate allows also for their emergence above the plate; their failure occurring for $T \rightarrow 1+$ is associated with the recurrence of an unbounded LD displacement.

SBP18 demonstrated how the phenomenon of waves up- and downstream of the edge

for $T > 1$ is associated with pre-detachment and severely violates the considerations (I)–(III) and the notion of expansive branching. They finally disclosed non-uniqueness of the solutions due to an arbitrary phase shift far upstream, seemingly to be fixed by a yet missing further downstream condition. We are therefore still left with the two constraints (2.14g) in our consistent description of the flow continued downstream of the edge by virtue of (2.14). The first states that not only $A(X)$ but also $A'(X)$ is continuous at $X = 0$, so that we henceforth omit the signs in the arguments 0– and 0+ of A , expressing one-sided limits. The second guarantees strictly forward interacting flow upstream of the edge, thus $A_0 > 0$ in (2.16). Since τ given in table 1 and J by (2.8) yields $T \lesssim 10$, assuming $T < 1$ is acceptable with regard to the last comment in § 2.2.

However, A becomes discontinuous at the edge by taking the limit $T \rightarrow 0$ in (2.14e) and (2.14h), implying the condensed interaction ($P' \equiv 0$) for $X > 0$. Here the possibility of free interaction exists but the conditions at $X = 0$ do not provoke it even upstream of the edge in the formal limit $G - P_- = T = 0$: then the classical Goldstein wake (Goldstein 1930) is recovered immediately downstream as the trivial solution $[\Psi, P] \equiv [Z^2/2, 0]$, representing the oncoming base flow, applies upstream of it.

3. Inviscid detachment at smaller scales

As emphasised in more detail below, the interactive flow structure leaves us with a still singular transition from no- to free slip. It therefore initiates its own breakdown on scales much smaller than the interactive ones. The bottom line of the subsequent analysis is that: demonstrating self-consistency of the interaction theory and a required smooth behaviour of all flow quantities at the edge demands a thorough analysis of the smaller scales. This will also highlight the strikingly different characteristics of the gross break-away of the film, i.e. the formation of a free streamline at the solid wall, in the present situation and (well-understood) steady internal separation: in the first, the flow quantities appear to undergo weak algebraic singularities, whereas in the second their behaviour is well-known to be regular at separation (Goldstein 1930).

Visualising the process of scale separation in figure 4 serves to illustrate the subsequent analysis of the different flow regimes, where figure 4(f) recovers the linkage to the teapot effect as in figure 2.

3.1. The influence of capillarity

To advance further in completing the description of flow detachment, it proves useful to first summarise the analysis in SBP18 of the interplay of surface tension and the Goldstein wake in the non-interactive limit $x \rightarrow 0+$. Then the latter exerts a displacement $-ax^{1/3}$ with some constant $a > 0$ ($a \simeq 1.0079$ if ψ_0 is given by Watson’s profile) on its top: $\psi \sim \psi_0(z) + ax^{1/3}\psi'_0(z) + O(x^{2/3})$. Accordingly, (2.3c), (2.6) and the Prandtl shift in (2.11) yield $[h_-, h_+] \sim [a_-, a_- - a]x^{1/3} + O(x^{2/3})$ with some sought constant a_- , and (2.3b) states that $p_y + g \sim \epsilon^2(a - a_-)(x^{1/3})''\psi_0^2(y)$. By integration across the unperturbed layer, from $y = 0$ to $y = h_0$, one finally obtains from (2.3e) the limiting overall capillary pressure jump in the form $(a - a_-)x^{1/3} \sim -T(h_- + h_+)$, i.e. $T(2a_- - a) = a_- - a$. This finally implies $[h_-, h_+] \sim ax^{1/3}[1 - T, T]/(1 - 2T)$. One first draws the important conclusion that $h_-(x)$ is to be regularised on interactive and again on smaller scales even for $T \geq 0$, whereas $h'_+(x)$ (> 0) remains indeed continuous at $x = 0$ for $T = 0$ as the inverse Prandtl shift produces additional irregular terms in the core region for $x \rightarrow 0+$ and a cuspidal distortion of $h_+(x)$ for $T > 0$ only. Even then, however, the regularisation of $h_+(x)$ is left to higher orders over the interaction x -scale,

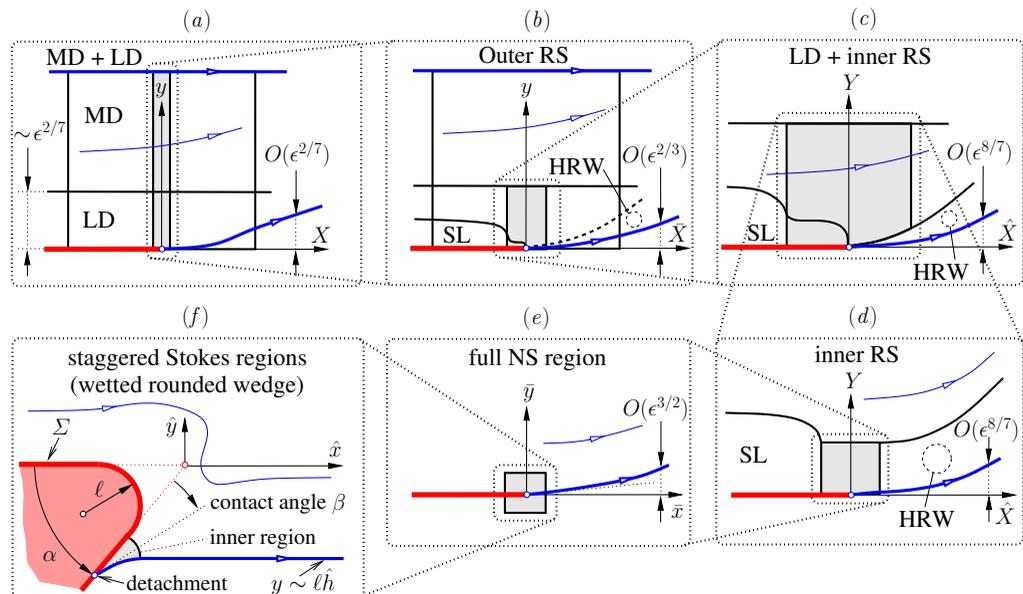


FIGURE 4. Essential flow regions, shaded details zoomed-in consecutively from (a) to (f) (not to scale, new denotations provided in § 3.3.1, § 4.1, § 3.3.3, § 4.3): flow detachment viewed on interactive down to smallest scales, where the free streamline is no longer elongated and the flow no longer slender; HRW as sublayer of LD (dashed boundary) but not as part of inner RS; for enhanced visibility, blue: free and internal streamlines and detachment point, red: plate and original tip coinciding with origin and detachment point, becoming separated in the situation resolved in (f).

where it is accomplished by the introduction of a thin shear layer adjacent to the upper free surface in order to satisfy (2.3d) (cf. SBP18, § 3.3.4).

It is noteworthy to highlight the difference to the related classical situation of the gravity- and capillarity-free axisymmetric flow exiting a pipe (Tillett 1968): there symmetry cancels the leading-order displacement in the core region but the vorticity gradient of the Hagen–Poiseuille profile (as opposed to streamline curvature) provokes an higher-order displacement and vertical pressure, requiring a regularisation similar to that discussed below.

Keeping in mind the above preliminary considerations applying to arbitrarily small values of T , we consider the precise regularisation of h_{\pm} for finite values of T . To this end, we first reappraise the interaction under the first of the restrictions (2.14g). The details of the detached flow in the close vicinity of the edge as reported by SBP18 provide an insight how the full interactive structure is recovered for $\epsilon^{9/14} \ll X = O(T^{3/8})$. In general, the so-called near-near wake, replacing the pressure-free Goldstein near-wake, emerges as a subregion split off the main portion of the LD to absorb the nonlinearity of the interaction immediately downstream of the trailing edge. Most importantly, it dictates the onset of free slip according to (2.14b).

3.2. Extended Hakkinen–Rott wake

As the second of the ICs (2.14h) requires $A - A(0) = O(X)$ ($X \rightarrow 0$), the near-near wake must suppress any larger contribution to A , hence transferred passively through the core of the LD. By this leading-order analysis, this wake itself then provides an example of condensed interaction and interesting, capillarity-controlled specification of the pressure-driven Hakkinen–Rott wake (HRW, Hakkinen & Rott 1965): P vanishes

as $X \rightarrow 0$ in an irregular manner such that the wake exerts zero displacement. Since the canonical pressure gradient in the HRW turns out to be adverse, P grows and, according to the capillary pressure jump (2.14d), the, at $X = 0$, curvature-free, just detached streamline becomes convex and bends vertically upwards as X grows. The strong pressure rise provokes an enhanced streamline curvature and this in turn the aforementioned breakdown and smoothing of the interaction theory for sufficiently small values of X , as already indicated in figure 1. In the LD, this is fully understood if one considers only the behaviour of the leading-order quantities Ψ and P , i.e. under the neglect of the vertical pressure variations.

The flow profile in the HRW matches that at detachment on its top in its limiting form given by (2.16). As a result, the self-preserving flow in the HRW discerned for $X \rightarrow 0+$ resolves the non-uniformity of (2.16). It is expressed as the inner limit

$$\left[\frac{\Psi}{\Lambda_0^{1/3} X^{2/3}}, \frac{\Delta P}{\Lambda_0^{4/3} X^{2/3}}, \frac{H_-}{\Lambda_0^{4/3} X^{8/3}} \right] \sim \left[f_{\text{HR}}(\eta), p_{\text{HR}}, \frac{9 p_{\text{HR}}}{40} \frac{1-T}{T} \right], \quad \eta := \frac{\Lambda_0^{1/3} Z}{X^{1/3}}, \quad (3.1)$$

with the pressure difference ΔP introduced in (2.14d). Here the universal wake function f_{HR} satisfying $f_{\text{HR}}^2 - 2f_{\text{HR}}f_{\text{HR}}'' = -2p_{\text{HR}} + 3f_{\text{HR}}''$, $f_{\text{HR}}(0) = f_{\text{HR}}''(0)$ and the matching condition $f_{\text{HR}}' \sim \eta + \text{TST}$ as $\eta \rightarrow \infty$ is recalled. Here the absence of a constant term determines the eigenvalue p_{HR} and prevents A from being of $O(X^{1/3})$ as $X \rightarrow 0+$ and enforces continuity of A' as required by (2.14h). Our refined numerical study yields $p_{\text{HR}} \simeq 0.61334$ and a rescaled free slip $f_{\text{HR}}'(0) \simeq 0.89915$ for $\max(\eta) = 50$ (cf. Hakkinen & Rott 1965, SBP18). This gives $U_s \sim f_{\text{HR}}'(0)X^{1/3}$ ($X \rightarrow 0+$) in (2.15) when rewritten in the limit $\eta \rightarrow 0$.

Next, we claim the regular/singular upstream/downstream behaviour including higher orders

$$\Delta P \sim \begin{cases} P'(0-)X + P''(0-)X^2/2 + O(X^3) & (X \rightarrow 0-), \\ p_{\text{HR}}\Lambda_0^{4/3}X^{2/3} + c_1X \ln X + c_2X + O(X^{4/3}(\ln X)^2) & (X \rightarrow 0+) \end{cases} \quad (3.2)$$

with the logarithmic variations and the constants c_1, c_2 to be determined through a higher-order analysis of the HRW. Accordingly, from (2.14e-g) or (2.17),

$$A - A(0) \sim A'(0)X + (G - P_-)\frac{X^2}{2} + \begin{cases} O(X^3), \\ \frac{9 p_{\text{HR}}}{40} \frac{1-2T}{T} \Lambda_0^{4/3} X^{8/3} + O(X^3 \ln X). \end{cases} \quad (3.3)$$

Our expectation of a more nonlinear theory superseding the current one when T crosses $1/2$ complies with the sign change of the singular contribution to A provided by the HRW. That weak downstream irregularity is also transferred to H_+ , cf. (2.11), as

$$H_+ \sim -A(0) - A'(0)X - (G - P_-)\frac{X^2}{2} + \begin{cases} O(X^3), \\ (9 p_{\text{HR}}/40)\Lambda_0^{4/3} X^{8/3} + O(X^3 \ln X). \end{cases} \quad (3.4)$$

By the expansive type of interaction for $S = -1$, $A(X)$ bends convexly but $P(X)$ concavely throughout (SRP18). That is, we deal with $A(0) > 0$, $A'(0) > 0$, but $P'(0-) < 0$.

One infers from (2.14c) that the i -th ($i = 1, 2, \dots$) contribution to the expansion for $\Psi - \Psi_0$ as $X \rightarrow 0$ attains the form $d_i(X)Z + e_i(X) + \text{TST}$ as $Z \rightarrow \infty$ where the series of gauge functions d_i and e_i are determined by the expansions (3.2) and (3.3) and add up to respectively $A(X) - A(0)$ and $[A(X)^2 - A(0)^2]/2 + P(X)$. Typically, $e_i(X)\Psi_0'(Z)$ are the eigensolutions of the linearised convective operator in (2.14a). By matching Ψ in the LD and the MD, the solution of the inviscid version of (2.14a) indeed yields the accordingly

refined form of the expansion for Ψ given by SBP18 (as (3.2), correctly including the logarithmic terms): with ΔP expanded as in (3.2), we have for

$$X \rightarrow 0\pm: \quad \Psi - \Psi_0 - A'(0)X \Psi_0'(Z) \sim \Delta P \Psi_0' \int_Z^\infty \frac{dt}{\psi_0'^2(t)} \sim \Delta P \begin{cases} 1 & (Z \rightarrow \infty), \\ 1/\Lambda_0 & (Z \rightarrow 0). \end{cases} \quad (3.5)$$

A detailed higher-order analysis of the HRW demonstrates self-consistency of the interactive asymptotic structure for $X \rightarrow 0$. Amongst other, it fixes the dependence of the coefficients c_1, c_2 in (3.2) on the parameters characterising the LD flow in the limit $X \rightarrow 0-$. Here we refer the interested reader to appendix A.

The breakdown and regularisation of the interactive flow structure for sufficiently small values of X is due to an unbounded vertical flow component and vertical pressure gradient evoked by the $O(X^{2/3})$ -term in (3.2) and (3.5) and the associated $O(X^{3/8})$ -term in (3.3). As a crucial observation, even then the pressure gradient in the HRW stays imposed by the flow on its top and must vary such that a potential singular displacement varying with $X^{1/3}$ is suppressed. Since the self-similar structure of the HRW already absorbs this type of condensed interaction and is recovered at its origin closer to the trailing edge, (3.1) prevails even over an x -scale much smaller than the interactive one. As an important finding, h_- is still given by (3.1) below.

3.3. Outer and inner Euler regions

We therefore consider two nested square outer and inner vortical-flow regions (when measured by the equally scaled global horizontal and vertical coordinates x and ϵy) that supersede locally the MD (outer) and the LD (inner) but where $\psi \sim \psi_0$ and $\Psi \sim \Psi_0$ still govern the flow at leading order. The associated linearised Euler or Rayleigh (RS) stages account for the small-scale upstream influence, embedded in that on the interactive scale, and serve to regularise the singular behaviour predicted in §3.2; most importantly, $h_+(x)$ by virtue of H_+ (outer). It is furthermore noted that the aforementioned large- Z representation of the expansion (3.5) accompanies a passive re-ordering of its hierarchy, so as to match the small- X limit of (2.11) provided by (3.3). Accordingly, the last expansion enforces a contribution of $O(X^{3/8})$ to (3.5) and this in turn a pressure-driven one of $O(X^{2/3})$ to the non-interactive disturbance of $O(\epsilon^{4/7})$ in (2.11).

3.3.1. Preliminaries

The introductory considerations lay the foundation for the outer and the inner mechanism of the further regularisation of the HRW, as follows.

(a) The interactive u - and p -variations, on account of streamline curvature via the vertical pressure variation in (2.3b), are of respectively $O(\epsilon^{2/7}X^{8/3})$ and $O(\epsilon^{4/7}X^{2/3})$ as $X \rightarrow 0+$. They and the non-interactive u -perturbation in (2.11), provoked by the streamwise pressure variation through (2.3a), all become of $O(\epsilon^{2/3})$ in the outer RS (§3.3.2) where, cf. (2.13),

$$\bar{X} := x/\epsilon = X/(l\epsilon^{1/7}) = O(1). \quad (3.6)$$

(b) Conversely, v of $O(\epsilon^{5/7}X^{-1/3})$ grows significantly to become comparable in size to the u -perturbation of $\epsilon^{2/7}X^{2/3}$ across most of the LD for $X = O(\epsilon^{3/7})$, i.e. in the inner RS (§3.3.5) where

$$\hat{X} := x/(m\epsilon^{9/7}) = X/(lm\epsilon^{3/7}) = O(1). \quad (3.7)$$

However, as p and ψ of $O(\epsilon^{2/3})$ at its base and downstream of the edge are still prescribed by the HRW, the inner RS cannot regularise the associated singularity expressed by (3.2)

and (3.5). Therefore, the analysis of inner RS is of only subordinate importance compared to that of the outer one.

(c) A quick justification of the expansions of the flow quantities below for both square regions relies on the relevant inviscid-flow approximation of the elliptic vorticity transport equation, obtained from elimination of the pressure in (2.3a,b):

$$\psi_{yy} + \epsilon^2 \psi_{xx} \sim -\Omega(\psi) := \psi_0''(\psi_0^{-1}(\psi)). \quad (3.8)$$

To express Ω as the vorticity conserved along the streamlines, we use ψ_0^{-1} to symbolise the inversion of the corresponding leading-order relationship $\psi \sim \psi_0(y)$. As a consequence, the contributions to those expansions are triggered by the vorticity impressed by the surrounding interactive flow and, in addition, the vorticity produced by the HRW and entering via non-trivial matching or BCs: at the base of the outer RS, provided by (3.5) with (3.2) for $Z \rightarrow \infty$; on top of the inner RS and at its base, here given by matching (3.5) for $T \rightarrow 0$ and (3.1). Consequently, eigensolutions of the linearised operator in (3.8) are absent.

It is noteworthy that Stewartson (1968) discovered the generic advent of a linearised Euler or Rayleigh stage when he solved the (non-rigorous) Oseen approximation of the NS problem governing the unconfined flow in a small region around a trailing edge. There the imminent and far-reaching rigorous appreciation of viscous–inviscid interaction in subsonic flow (Stewartson 1969; Messiter 1970) on larger scales is already implicit.

3.3.2. Outer Rayleigh stage: main deck

In the outer square region, p is, as in the surrounding MD, of $O(\epsilon^{4/7})$, and the viscous terms in (2.3a,b) become formally of $O(\epsilon)$ as all remaining ones can be scaled to $O(1)$. Following the comments (a) and (c) above, substitution of (3.3) into (2.11) suggests, in this domain, the expansion $\psi \sim \psi_0(y) + \epsilon^{2/7}\psi_1(y) + \epsilon^{3/7}\psi_2(y) + \epsilon^{4/7}\psi_3(y) + O(\epsilon^{4/6})$. The sought functions $\psi_{1,2,3}$ satisfy the hierarchy of Rayleigh equations

$$(\partial_{yy} + \partial_{\bar{X}\bar{X}} - \psi_0'''/\psi_0')\psi_{1,2} = 0, \quad (\partial_{yy} + \partial_{\bar{X}\bar{X}} - \psi_0'''/\psi_0')\psi_3 = \psi_1^2(\psi_0'''/\psi_0')/(2\psi_0') \quad (3.9)$$

ensuing from expanding (3.8). According to the considerations following (3.8) and the regularity of (2.11) upstream of the trailing edge, $\psi_{1,2}$ consist just of the pressure-free disturbances given by the Taylor series of $A(X)$ up to second order, where $A''(0-) = G - P_-$ from (2.14e) subject to (2.14h). This and the inhomogeneity in the last equation in (3.9), caused by the inertia-based nonlinearities, require an additional y -dependent component of ψ_3 .

Specifying these findings gives

$$[\psi, h_+] \sim [\psi_0(y), h_0] + m[\epsilon^{2/7}A(0) + \epsilon^{3/7}A'(0)l\bar{X} + \epsilon^{4/7}(G - P_-)(l\bar{X})^2/2][\psi_0'(y), -1] \\ + \epsilon^{4/7}m[\psi_*(y), -\psi_*(h_0)/u_0^+] + \epsilon^{4/6}[\bar{\Psi}(\bar{X}, y), \bar{H}(\bar{X})] + O(\epsilon^{5/7}). \quad (3.10)$$

Hence, ψ_* denotes the limiting value of the corresponding $O(\epsilon^{4/7})$ -contribution to the expansion (2.11) of ψ in $X = 0$. That quantity satisfies $\psi_*'' - (\psi_0'''/\psi_0')\psi_* = (\psi_0'''/\psi_0')A(0)^2/2 - A''(0-)\psi_0'$, where the last inhomogeneity reflects the action of the streamwise pressure gradient. We furthermore expand

$$p \sim \epsilon^{4/7}ml^2 \left[(G - P_-) \int_0^y \psi_0'^2(t) dt - M \left(\frac{Gy}{h_0} - P_- \right) \right] + \epsilon^{4/6}\bar{P}(\bar{X}, y) + O(\epsilon^{5/7}). \quad (3.11)$$

The X -independent leading-order term in (3.11) is again just the dominant contribution to p in the MD up- and downstream of the trailing edge, cf. SBP18, evaluated at $X = 0$ and rewritten with the aid of (2.9). Here the irregular terms in (3.3) play no

role. It follows from inserting (3.10) into (2.3b) and integrating its thereby reduced form $p_y \sim \epsilon^{4/7} m l^2 \psi_0'^2 - g$ subject to $p \sim p_-$ as $y \rightarrow 0$, to match p in the LD. Moreover, (3.10) fulfils (2.3c) supplemented with (2.6) and, together with (3.11), complies with the capillary pressure jump at $y = h_+$ in (2.3e) up to $O(\epsilon^{4/7})$ for $\bar{X} = O(1)$. The $O(\epsilon^{4/6})$ -contributions to (3.10), (3.11) serve to regularise the flow quantities in the MD. As the subsequent analysis of $\bar{\Psi}$, \bar{H} , \bar{P} makes clear, those expansions do indeed not contain lower-order eigenfunctions having sufficiently strong decay for $|\bar{X}| \rightarrow \infty$, consistent with (2.11).

Invoking the inverse Prandtl shift in (3.10) gives $\psi_0(y) \sim \psi_0(z) + h_- \psi_0'(z)$ for $h_- = O(\epsilon^{2/3})$, see (3.4), and brings to mind matching ψ up to $O(\epsilon^{2/3})$ in (2.11) and also in the LD, according to (3.5) and (3.2). Furthermore, $\bar{\Psi}$, \bar{P} are seen to satisfy the linearised Euler equations

$$\psi_0'' \bar{\Psi}_{\bar{X}} - \psi_0' \bar{\Psi}_{y\bar{X}} = \bar{P}_{\bar{X}}, \quad \psi_0' \bar{\Psi}_{\bar{X}\bar{X}} = \bar{P}_y. \quad (3.12)$$

To separate the influence of the shear stress at detachment, Λ_0 , effective in the LD and of a potential \bar{X} -independent contribution to $\bar{\Psi}$ arising from integration of (3.12) (i.e. no $O(\epsilon^{2/3})$ -contribution to Ω , cf. (3.8), in the surrounding MD), we advantageously consider the scaled vertical flow perturbation

$$\bar{V} := -\bar{\Psi}_{\bar{X}}/\bar{\Lambda}, \quad \bar{\Lambda} := 2p_{\text{HR}} \lambda^{1/3} \Lambda_0^{4/3}/3. \quad (3.13)$$

Equations (3.12) yield the Rayleigh equation governing \bar{V} in accordance with (3.9):

$$(\partial_{yy} + \partial_{\bar{X}\bar{X}} - \psi_0'''/\psi_0')\bar{V} = 0. \quad (3.14a)$$

Matching ψ and p in the outer RS and the LD with the support of (2.12) and m, l given by (2.11), (2.13) requires for

$$y = 0: \quad \bar{V} = -\theta(\bar{X})\bar{X}^{-1/3}. \quad (3.14b)$$

Furthermore, expanding (2.3c) and (2.3e) gives

$$\bar{H} = -\bar{\Psi}(\bar{X}, h_0)/u_0^+ \quad (3.14c)$$

and $\bar{P}(\bar{X}, h_0) = -\tau \bar{H}''(\bar{X})$ respectively. By the same token, inspection of (3.12) with the help of (2.6), (2.9) and (3.14c) gives for

$$y = h_0: \quad u_0^{+2} \bar{V}_y = -T J \bar{V}_{\bar{X}\bar{X}}, \quad (3.14d)$$

i.e. the explicit dependence of \bar{V} on T . Also, matching (3.10), (3.11) with (2.11) and p in the MD subject to (3.3) and (3.2) yields $\bar{\Psi} \rightarrow 0$ and $\bar{P} \rightarrow 0$, thus $\bar{V} \rightarrow 0$ and $\bar{H} \rightarrow 0$ by (3.14c), as $\bar{X} \rightarrow -\infty$. In contrast, $\epsilon^{2/3} \bar{\Psi}$ for $\bar{X} \gg 1$ must match the dominant singular behaviour of $\psi - \psi_0 \sim \epsilon^{2/7} m (A - H_-)(X) \psi_0'(y)$ for $X \ll 1$ as inferred from (2.11). From (3.1), (3.3) and $\psi - \psi_0 \sim -(9p_{\text{HR}}/40)\epsilon^{2/3} m \Lambda_0^{4/3} (L\bar{X})^{8/3}$ follows eventually $\bar{V}/\psi_0'(y) \sim 9\lambda \bar{X}^{5/3}/(10M) + O(\bar{X}^{-1/3})$ ($\bar{X} \rightarrow \infty$). Likewise, (3.13) and (3.14c) give $\bar{H}/\bar{\Lambda} \sim 27\lambda \bar{X}^{8/3}/(80M) + O(\bar{X}^{2/3})$. This proves consistent with the interplay of the two free surfaces in §3.2.

It is illuminating to demonstrate that the up- and downstream asymptotes are already intrinsic to the problem (3.14) governing $\bar{\Psi}$ and \bar{H} . To this end, we consider the weakest admissible, i.e. first algebraic, decays of \bar{V} for $\bar{X} \rightarrow \pm\infty$ with unknown dominant corresponding rates $\bar{a}_\pm(\bar{X})$, say. We obtain from (3.14a,b), using $(\partial_{yy} - \psi_0'''/\psi_0')\bar{V} \equiv (\psi_0' \bar{V}_y - \psi_0'' \bar{V})/\psi_0'$ and standard methods and (2.5), the long-wave approximation of \bar{V}

$$\frac{\bar{V}}{\psi_0'(y)} \sim \bar{a}_\pm + \bar{a}_\pm' \left[\bar{b}_\pm - \int_0^y \frac{dt}{\psi_0'^2(t)} \int_0^t \psi_0'^2(s) ds \right] - \frac{\lambda\theta(\bar{X})}{\bar{X}^{1/3}} \int_y^{h_0} \frac{dt}{\psi_0'^2(t)} + O(\bar{a}_\pm''''', \bar{X}^{-7/3}) \quad (3.15)$$

where \bar{a}_\pm and the constants \bar{b} are determined by solvability conditions of the inhomogeneous problems governing the $O(\bar{a}_\pm'')$ - and the $O(\bar{a}_\pm''')$ -term respectively. The small- y behaviour of ψ_0 in (2.5) grants a corresponding regularity of the right-hand side of (3.15). Substitution of (3.15) into (3.14d) using (2.5) and (2.6) gives, after division by u_0^+ , the solvability relation $\bar{a}_\pm'' J - \lambda\theta(\bar{X})\bar{X}^{-1/3} \sim \bar{a}_\pm'' \tau$. In the upstream case, this statement can only be met in the limit $T \rightarrow 1-$, cf. (2.9). Consequently, $\bar{a}_- \equiv 0$, $\bar{b}_- = 0$, and the upstream decay is indeed exponential, where the limit of an undamped (neutral or harmonic) oscillation is as also taken into consideration and an unbounded increase of \bar{V} is expected for $T \rightarrow 1-$. In contrast,

$$\bar{a}_+ = 9\lambda\bar{X}^{5/3}/[10J(1-T)] \quad (3.16)$$

confirms the aforementioned leading-order asymptote involving M defined in (2.9). This shows that matching (3.10) and (2.11) requires $T < 1$.

As a further result, (3.12) yields

$$\bar{P} = \psi_0''\bar{\Psi} - \psi_0'\bar{\Psi}_y, \quad (3.17)$$

and $\bar{P} \sim 3\lambda\bar{X}^{2/3}/2$ ($\bar{X} \rightarrow \infty$) provides the match of p in the MD, according to (3.2), (3.5) and (3.14b). This and $\bar{P}(\bar{X}, 0) = 3\lambda\bar{X}\theta(\bar{X})\bar{X}^{2/3}/2$ make evident how $\bar{\Psi}$ and \bar{P} resort to these behaviours originating in the HRW and why the inner RS is required to complete the regularisation closer to the trailing edge. Since the coefficient ψ_0'''/ψ_0' in (3.14a) becomes, cf. (2.5), ωy for $y \ll 1$, (3.14b) allows \bar{V} to attain an undesired potential-flow pole in the origin, as described by the singular eigensolutions of the Laplacian $r^{-N} \sin(N\vartheta)$ where

$$r := \sqrt{\bar{X}^2 + y^2} \rightarrow 0, \quad 0 \leq \vartheta := \arctan(y/\bar{X}) \leq \pi \quad (3.18)$$

and $N > 0$ is some integer (cf. Scheichl 2014). Its occurrence has to be avoided in the further treatment of (3.14). Rather, (3.14b) and the vorticity term provoke a weaker singularity as one readily finds that

$$\bar{V} \sim \bar{V}_0 + \bar{c}_1 y + \bar{c}_2 xy + O(r^{8/3}) \quad (r \rightarrow 0), \quad \bar{V}_0 := 2r^{-1/3} \sin(\pi/3 - \vartheta/3)/\sqrt{3}, \quad (3.19)$$

and (3.17) recovers the pressure induced by the HRW as $\bar{P} = O(r^{2/3})$. The first three contributions to \bar{V} in (3.19) are of potential-flow type, and the coefficients $\bar{c}_{1,2}$ of the homogeneous ones are determined by the overall solution for \bar{V} . The (lengthy expression of the) $O(r^{8/3})$ -term in (3.19) solves the Poisson problem to which (3.14a) reduces to with $\psi_0'''\bar{V}/\psi_0' \sim \omega y\bar{V}_0$ forming the inhomogeneity. The singularity described by \bar{V}_0 is pivotal in §3.3.5 where it comes to its regularisation by the inner RS.

For what follows, we introduce the Fourier transform of a function $f(\bar{X}, y)$ for complex wavenumbers k ,

$$\phi\{f\}(k, y) = \frac{1}{2\pi} \int_{-\infty}^{\infty} f(\bar{X}, y) e^{-ik\bar{X}} d\bar{X}. \quad (3.20)$$

We first assume that \bar{V} decays exponentially far upstream. Since it grows with $O(\bar{X}^{5/3})$ as \bar{X} becomes large, (3.20) defines $\phi\{\bar{V}\}$ first in the open strip $-\mu_1(T) < \text{Im } k < 0$ where $-\mu_1$ denotes the imaginary coordinate of the pole in the lower half-plane $\text{Im } k \leq 0$ lying closest to the real axis. The analytic continuation of \bar{V} into the entire k -plane excluding the locations of singularities is provided by the convenient decomposition

$$\phi\{\bar{V}\}(k, y) = \mathcal{B}(k)\mathcal{V}(k, y), \quad \mathcal{B}(k) := \phi\{\theta(\bar{X})\bar{X}^{-1/3}\}(k) = 1/[\sqrt{3}\Gamma(\frac{1}{3})(ik)^{2/3}]. \quad (3.21)$$

The last expression is understood in connection with a branch cut along the positive imaginary k -axis. Absorbing (3.14b) and accommodating the non-integer growth with \bar{X}

in (3.16), it captures the influence of the HRW and gives a non-trivial \bar{V} . Poles of \mathcal{V} on the real k -axis allow for relaxing the original assumption of exponential decay by the inclusion of harmonic modes surviving far upstream. From (3.14) we deduce the Rayleigh equation

$$(\partial_{yy} - k^2 - \psi_0'''/\psi_0')\mathcal{V} = 0 \quad (3.22a)$$

subject to the then inhomogeneous lower and the homogeneous upper BC,

$$y = 0: \quad \mathcal{V} = -1, \quad (3.22b)$$

$$y = h_0: \quad \psi_0'^2 \mathcal{V}_y = T J k^2 \mathcal{V}, \quad (3.22c)$$

cf. (2.5). The solution of the two-point boundary value problem (3.22), parametrised by k , facilitates the semi-analytical inversion of (3.20) so as to determine \bar{V} , parametrised by $\psi_0(y)$ and T , in an elegant manner, avoiding the above-mentioned Laplacian eigen-solutions; all the more, as our focus lies on $\bar{H}(\bar{X})$ given by (3.14c). For the numerical implementation of (3.22), we recall that ψ_0 is specified by Watson's (1964) flow profile. In turn, the properties (2.6), (2.7) and the closed form of ψ_0 in Scheichl & Kluwick (2019) and the values for $J = \lambda$ and u_0^+ given by (2.8) are employed. Detailing the properties of (3.22), especially the behaviours of \mathcal{V} for $k \rightarrow 0$ and $|\operatorname{Re} k| \rightarrow \infty$ and the analysis of its poles, which select the discrete spectrum of \bar{V} out of the continuous (and where (3.22) does not have a solution but its homogeneous form does), is relegated to appendix B. These findings enable the representation of \bar{V} in most efficient manner as envisaged next.

The poles of \mathcal{V} lie symmetrically with respect to both the real and the imaginary k -axes. There are a double pole in $k = 0$, exactly two real single poles where $k = \pm k_u(T)$ with $k_u > 0$ (§ B.1) and an infinite number of single poles lying on $k = \pm i\mu_i(T)$ ($i = 1, 2, \dots$) with $\mu_i > 0$ (§ B.3). Since $\mathcal{V}(-k, y) \equiv \mathcal{V}(k, y)$, $\operatorname{Res}_{k=-k_u}(\mathcal{V}) = -\operatorname{Res}_{k=k_u}(\mathcal{V})$ and real, and $\operatorname{Res}_{k=-i\mu_i}(\mathcal{V}) = \operatorname{Res}_{k=i\mu_i}(\mathcal{V})$ and imaginary. We then have

$$\left[\bar{V}, \frac{\bar{\Psi}}{\bar{A}} \right](\bar{X}, y) = \int_{\mathcal{C}} \mathcal{B}(k) \mathcal{V}(k, y) e^{ik\bar{X}} \left[1, \frac{i}{k} \right] dk \quad (3.23)$$

where all possible paths of integration \mathcal{C} stretch from $\operatorname{Re} k = -\infty$ to $\operatorname{Re} k = +\infty$ and originate from one another through a continuous deformation as they divide the k -plane in two portions: the origin and all poles $k = i\mu_i(T)$ lie in the upper and all poles $k = -i\mu_i(T)$ in the lower part. We furthermore anticipate that both real poles are located either in the upper or the lower part to guarantee \bar{V} being real. Indeed, as will be argued below to render \bar{V} unique, \mathcal{C} must bypass both real poles such that they lie in the lower part. This situation is sketched in figure 5 with the path \mathcal{C} specified for the numerical calculation of $\bar{H}(\bar{X})$ by means of (3.23) and (3.14c) for $\bar{X} \geq 0$. There the branch cut prevents a more efficient treatment of (3.23) using Cauchy's residue formula: to avoid accuracy issues associated with complex integration, we specified \mathcal{C} to follow the real axis apart from small squares of lengths 2ε with the midpoints $k = \pm k_u$ and of length ε with the midpoint in the origin. Consistency of the results is confirmed for values of ε ranging from 0.1 to 0.3. On the other hand, applying Cauchy's residue theorem to (3.23) yields with (3.21), the fact that $\operatorname{Res}_{k=-k_u}(\mathcal{V}) = -\operatorname{Res}_{k=k_u}(\mathcal{V})$ and Euler's reflection formula after some algebra

$$\frac{\bar{\Psi}}{\bar{A}} = 2 \operatorname{Res}_{k=k_u}(\mathcal{V}) \frac{\cos(k_u \bar{X} - \pi/3)}{k_u^{5/3}} + i \sum_{i=1}^{\infty} \operatorname{Res}_{k=-i\mu_i}(\mathcal{V}) \frac{\exp(\mu_i \bar{X})}{\mu_i^{5/3}} \quad (\bar{X} \leq 0) \quad (3.24)$$

(cf. Tillett 1968). This series of residues converges (uniformly) for any $\bar{X} < 0$. The full

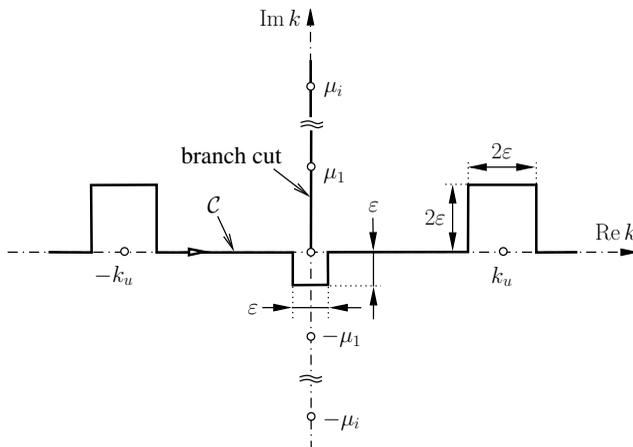


FIGURE 5. Sketch of k -plane: double-symmetric singular points (circles), actual path C and direction of integration.

evaluation of (3.23) and smoothness of $\bar{\Psi}$ for $y > 0$ in $\bar{X} = 0$ confirms that (3.24) holds even there although the decay of the exponentials has disappeared.

Finally, \bar{H} for $\bar{X} \leq 0$ follows from (3.14c) and directly from (3.24) in convenient manner. This approach allows for checking the accuracy of the full integration according to (3.23). It is definitely preferred for resolving most accurately the hitherto unprecedented, discrete undamped capillary Rayleigh modes forming a wave crest upstream of the edge we remarkably record: resorting to the real poles, these have wavenumbers $k = k_u$, found to strictly increase as T decreases. Here we point to the classical dispersion relation of small-amplitude capillary waves in a finite-depth layer of uniform parallel flow with uniform speed scaled to unity over a flat bed (see Drazin & Reid 2004, p. 30; VandenBroeck 2010, §2.4.2), directly obtained from the case of symmetric modes in (2.18) with $k/2$ replaced by k in the current setting. There stationary modes exist for the two wavenumbers $k = \pm k_u$ satisfying $1 = T k_u \tanh k_u$. Here we extract from (3.24) the neutral amplitude normalised with A

$$\bar{a}_u := 2\Gamma\left(\frac{2}{3}\right) \operatorname{Res}_{k=k_u}^s [\mathcal{V}(k, h_0)] / (u_0^+ k_u^{5/3}). \quad (3.25)$$

To compute (3.23) (for $y = h_0$), we restrict the numerical integration to the interval $|\operatorname{Re} k| \leq 20$, which in view of the exponential large- k tails of \mathcal{V} (§B.2) gives satisfactorily accurate results. (Specifically, we find $\mathcal{V}(k, h_0) \sim \exp(-|k|h_0)$). The evaluation of the integrand employs a cubic-spline interpolation of the solution \mathcal{V} of the Rayleigh problem (3.22) for discrete values of k . We advantageously mitigated the singularity at $k = 0$, circumvented at a small distance (see figure 5), by splitting off the first two terms in the small- k expansion of $\mathcal{V}(k, h_0)$ and finally adding their inverse Fourier transform, resulting in the reciprocal large- \bar{X} representation of \bar{V} (§B.1) and \bar{H} via (3.23). We skip the details of this alternative derivation of (3.15) in its more complete form, supplemented with (3.16), also yielding the according asymptote of \bar{H} by integration. To evaluate (3.24) (for $y = h_0$) and discrete \bar{X} -values, the poles of \mathcal{V} are detected as the roots $k = k_p$, say, of $\mathcal{V}^{-1}(k, y)$. Since $\mathcal{V} \sim \operatorname{Res}_{k=k_p}(\mathcal{V}) / (k - k_p)$ as $k \rightarrow k_p$, the according residuals (given by a homogeneous solution to (3.22), see above) are computed as $1 / [\partial_k \mathcal{V}^{-1}(k_p, y)]$ ($y = h_0$). For $i > 7$ and \bar{X} lying not too close to zero, the values of the exponentials for have already fallen below the round-off error; a few more modes calculated using the asymptotic behaviour of the residuals (§B.3) were, however, added.

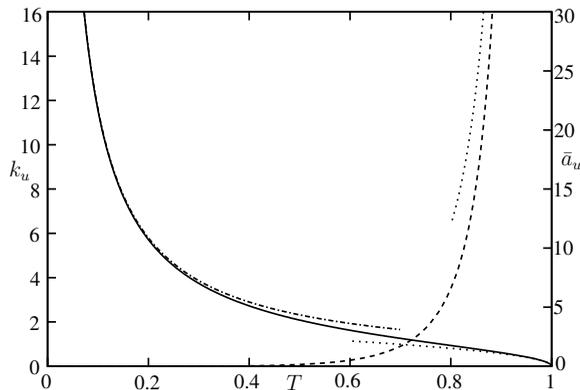


FIGURE 6. Wavenumber k_u (solid) and amplitude \bar{a}_u (dashed), see (3.25), of the neutral capillary mode vs. inverse Weber number T , asymptotes given in the appendix B: (B13)–(B15) (dotted); (B22) (dash-dotted).

The resulting plots in figures 6 and 7 also employ cubic-spline interpolation of the pointwise data sets. Figure 7(a) displays the results obtained by summation of residuals. As one expects, these are slightly more accurate for very negative values of \bar{X} and small values of T than those found by the direct evaluation of (3.23). Figure 7(b) indicates that excellent agreement with the asymptotes found analytically can be ascertained. It is seen that \bar{H} undergoes a trough immediately downstream of the edge before it recovers to assume rapidly the algebraic far-downstream growth described by (3.15), (3.16) and §B.1. In addition, (3.25), (B18) and (B23) imply the optimum estimate $\bar{a}_u = O(k_u^{-11/3} e^{-k_u h_0})$ as k_u becomes large. This corroborates the extremely rapid upstream decay of the Rayleigh modes found numerically as $T \rightarrow 0$. Even the maximum value of k_u shown lies on the part of \mathcal{C} considered for the numerical integration, but the suppression of exponentially growing terms in the calculation of \mathcal{V} and the residuals becomes a numerically delicate task when $|k|$ becomes sufficiently large. In the long-wave limit $k_u \rightarrow 0$ as $T \rightarrow 1^-$, $\bar{\Psi}$ diverges both immediately upstream of the trailing edge as \bar{a}_u grows like $k_u^{-14/3}$ and for constant but sufficiently large positive \bar{X} . Also these findings compare favourably with the curves in figure 7. The intriguing further implications of the long-wave limit are addressed in §5.

3.3.3. Why capillary undulations exist only upstream of the trailing edge

In fact, the decision whether the oscillatory capillary modes occur either up- or downstream of the trailing edge, depending on whether the real poles are part of the lower or upper part of the k -plane divided by \mathcal{C} , cannot be left to the present steady-flow analysis. In both cases, these small-scale Rayleigh waves are also manifest above the MD of the interactive flow, modulating their amplitude over the interactive streamwise length scale. We now catch up on the convincing (even though not rigorous) argument substantiating their presence upstream of the edge, as already anticipated in figure 1.

As inferred from the long-wave limit of (3.14a), the Rayleigh-type perturbation of the streamfunction ($\epsilon^{2/3}$) in (3.10) are morphed into a pressure-free one $\epsilon^{2/3} \bar{\psi}_y(\bar{X}, 0) \bar{\psi}'_0(Z)$ in the LD. It exhibits a rapid (harmonic) streamwise variation, either far up- or far downstream. Inspection of (2.3a) shows that typically a further viscous sublayer or slip layer (SL, figure 4b) where $Z = O(\epsilon^{1/21})$ is required on account of the no-slip BC. For very negative values of \bar{X} , this shear layer is of the type provoked by the rapid small-scale disturbances considered in SBP18; for $\bar{X} \ll \epsilon^{1/7}$ ($X \ll 1$), it becomes absorbed by

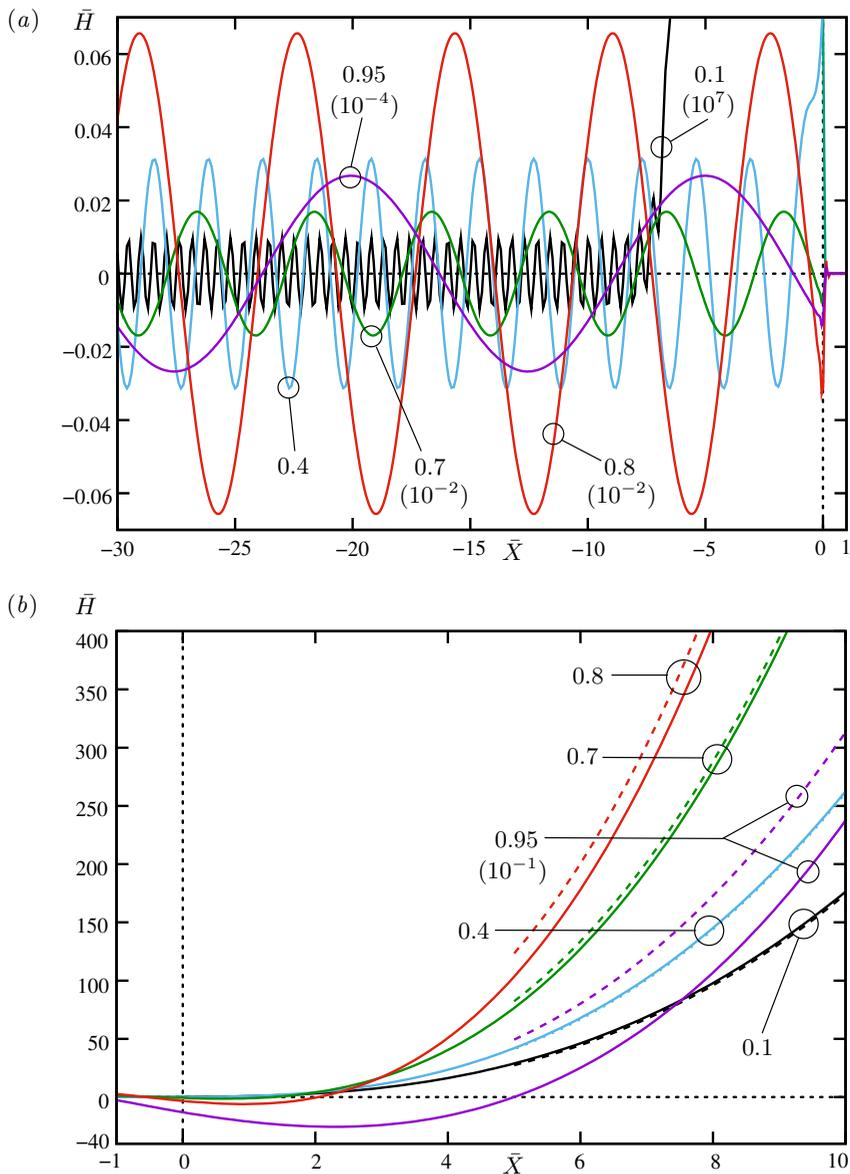


FIGURE 7. \bar{H} vs. \bar{X} and T (a) upstream, (b) downstream of trailing edge: labels indicate T -values; multiples $\neq 1$ of \bar{H} (in parentheses) shown for enhanced visibility; plot resolution of strongly augmented oscillations for $T = 0.1$ discerned in (a); two-terms downstream asymptotes (dashed) from (3.15) with (3.16).

the HRW, there serving as the viscous correction of the LD; for larger values of \bar{X} , an additional perturbation in the expansion of $-\epsilon^{2/3}\bar{\psi}_y(\bar{X}, 0)U_s(X)$ of h_- serves to satisfy the free-slip condition $\psi_{zz} \sim 0$ on $z = 0$ to which (2.3d) reduces to: see (2.15).

This inspection allows for the existence of the undular modes up- and downstream of the edge. That is, a steady-flow analysis can *not* rule out one of these two possibilities. We therefore justify our choice by making a recourse to the detection of capillary modes exclusively upstream of a wall-mounted obstacle, serving as a compact forcing, by Bowles & Smith (1992) and Rayleigh’s celebrated radiation principle, which exploits

the anomalous dispersion relation for small-amplitude capillarity waves. Acknowledging their essentially inviscid nature in both situations (despite their amplitude of $O(\epsilon^{2/3})$ here), we consider this analogy as reasonable.

As a serious objection, however, we have to admit that this principle applies strictly only to a uniform (potential) background flow, where it was adopted by [Cumberbatch & Norbury \(1979\)](#). The last authors also point to the rigorous justification of this observation by solving the signalling problem, following [DePrima & Wu \(1957\)](#). Applied to the current situation, this demands for the solution of the unsteady extension of (3.14a) subject to an artificial, spontaneous introduction of the trailing edge in the unperturbed flow described by ψ_0 . That is, one expects a pertinent neutral mode for zero frequency in the long-time response in the spectrum, to occur just up- rather than downstream of the edge. A less expensive modification of this ideal, rigorous approach is the introduction of artificial viscosity and tracing that particular wavenumber in the k -plane when the then complex frequency tends to zero (cf. [Huerre & Monkewitz 1990](#), § 3.4). This serves to single out the mode upstream as the physically meaningful alternative.

As the here sketched routes are felt to be beyond the scope of the present paper, they shall be pursued in a separate study.

3.3.4. Diffusive overlayer

Expansion (3.10) typically accounts also for the second dynamic BC (2.3d), requiring vanishing shear stress on the top free surface, up to $O(\epsilon^{3/7})$, i.e. as along as (2.3d) reduces to $\psi_{yy} \sim 0$ on $y = h_+$. Moreover, it was indicated in SBP18 how (2.3d) alters the highest-order contribution of $O(\epsilon^{4/7})$ to the inviscid flow described by (2.11) in a thin layer adjacent to the upper free streamline accounting for viscous diffusion in weak perturbations around the base flow. From inspection of (2.3a), it penetrates to values of $h_+ - y$ measured by the square-root of its horizontal extent and thus of $O(\epsilon^{3/7})$. Since the flow therein itself becomes inviscid over the shortened Rayleigh scale, a further diffusion layer of reduced vertical depth arises where \bar{X} and $\xi := (y - h_+)/\epsilon^{1/2}$ are of $O(1)$ and (2.3d) is formally retained in full. A comprehensive completion of the present self-consistent theory suggests a brief examination of this overlayer meeting (2.3d). This is relegated to appendix § C.

3.3.5. Inner Rayleigh stage: lower deck

Following the outline (b) at the end of § 3.3, the inner square region regularises P by taking into account the transverse variation of p , which becomes of $O(\epsilon^{6/7})$ according to (3.19) and (3.18) with (3.7). Then (3.10), (3.11) yield the here relevant expansion

$$[\psi, p - p_-] \sim \epsilon^{4/7}[(M^2/\lambda)^{1/7}\Psi_0(Y), 0] + \epsilon^{6/7}[\hat{\Psi}, \hat{P}](\hat{X}, Y) + O(\epsilon^{20/21}), \quad (3.26)$$

where we advantageously revert to the inverse Prandtl transposition in (2.13). Again, the quantities $\hat{\Psi}$, \hat{P} describe a linearised Euler flow, now with Ψ_0 providing the base profile. Therefore, $\hat{V}(\hat{X}, Y) := -\hat{\Psi}_{\hat{X}}$ satisfies a Rayleigh problem of the type (3.22) except for (3.14c), (3.14d) being replaced by the required decay for large values of $R := r/(m\epsilon^{2/7}) = (\hat{X}^2 + Y^2)^{1/2}$, where the displacement of the HRW controls \hat{V} by virtue of a $R^{-1/3}$ -variation matching (3.19). Since the absence of a free surface at play renders the Rayleigh operator here self-adjoint, all poles lie on the imaginary axis of the corresponding wavenumber plane, which suppresses oscillations of wavenumbers much smaller than those detected in § 3.3.2. Moreover, following the analysis leading to (3.19) recovers the far-field singularity also for $R \rightarrow 0$.

This shows that the inner RS fulfils its original task of regularising the pressure provoked by the HRW in the outer RS across the LD only unsatisfactorily, and the asso-

ciated Rayleigh problem does not merit a more detailed analysis as it proves physically insignificant.

Since the scaled slip $\bar{\Psi}_y(\bar{X}, 0)$ exerted by the outer RS becomes of $O(\bar{X}^{1/3})$ as $\bar{X} \rightarrow 0-$, the vertical extent of the associated slip layer (SL) introduced in § 3.3.3 shrinks typically to $Y = O(\epsilon^{1/21} \bar{X}^{1/3})$. It is continued as a sublayer covering the inner region where $Y = O(\epsilon^{1/7})$ (figure 4c). There the driving slip is replaced by $\hat{\Psi}_Y(\hat{X}, 0)$, which again attains a $\hat{X}^{1/3}$ -behaviour as $\hat{X}^{1/3} \rightarrow 0-$. We are therefore concerned with a collapse of the inner RS, the SL and the HRW into a single region (figure 4(d) addressed next.

4. Full Navier–Stokes and Stokes regions

As the conditions (2.14h) take into account the detachment of the lowermost streamline but not the egde as a geometric restriction or even its micro-geometry on the length scales considered so far, the prior analysis does not determine whether detachment occurs actually at the edge or further upstream. Therefore, this question is taken up first through an examination of even smaller scales, governing first a full NS regime. This ensues from a breakdown of (3.26) initiated by the unresolved singularity of \hat{P} , just discussed, and the associated unbounded growth of the vertical flow component, $-\hat{\Psi}_{\hat{X}}$. The associated growth of v evaluated in the HRW shows the emergence of the NS region. We will see that it embeds at least one Stokes region around detachment so that the flow can accommodate to the wetting properties controlling the emerging meniscus and defined by the thermodynamic three-phase equilibrium holding in the detachment point.

4.1. Leading-order problem over upper half-plane

The slender-flow approximation underlying (3.1) ceases to be valid where both u and v become of $O(\epsilon^{1/2})$ as $(\bar{x}, \bar{y}) := (x/\epsilon^{3/2}, y/\epsilon^{1/2})$ and, see (3.18), $\bar{r} := r/\epsilon^{1/2} = (\bar{x}^2 + \bar{y}^2)^{1/2}$ are of $O(1)$. In this half-plane $0 \leq \vartheta \leq \pi$, we expand

$$[\psi/\epsilon, (p - p_- + gy)/\epsilon, h_-/\epsilon^2] \sim [\bar{\psi}(\bar{r}, \vartheta), \bar{p}(\bar{r}, \vartheta), \bar{h}(\bar{x})] + O(\epsilon^{3/2}) \quad (4.1)$$

with the sought quantities $\bar{\psi}$, \bar{p} , \bar{h} of $O(1)$ as $\epsilon \rightarrow 0$. Due to the sufficiently smooth variation of the detached streamline beneath the HRW, this remains slender in the present NS region where

$$\bar{y} \sim \epsilon^{3/2} \bar{h}(\bar{x}) \quad \text{or} \quad \vartheta \sim \epsilon^{3/2} \bar{h}(\bar{x})/\bar{x}. \quad (4.2)$$

Consequently, $\bar{\psi}$, \bar{p} satisfy the full NS equations (2.3a,b) describing a perfectly supercritical flow in the upper half plane. This is subject to mixed, linear, homogeneous BCs implied by (2.3c–e) and a radiation condition which accounts for the externally imposed shear flow. From the reference capillary number in (2.2b), the reduced velocity scale $\sqrt{\epsilon} \tilde{U}$ and the relative flatness of the detaching streamline given in (4.2), the currently relevant capillary number $\epsilon^{1/2} Ca/\epsilon^{3/2} = 1/\tau$ of $O(1)$ implies the leading-order balance $2\epsilon^2 \psi_{yx} + p - p_- \sim \tau \varkappa_-$ retained in (2.3e). However, here the normal-stress jump across the fluid–gas interface evaluated at $\bar{y} = 0$ determines its small curvature $\varkappa_- \sim \epsilon \bar{h}''(\bar{x})$, which then has an only passive, higher-order effect on the flow. Accordingly, the weak vertical displacement of the former provokes the $O(\epsilon^{3/2})$ -correction in (4.1), for $\bar{x} \rightarrow \infty$ matching the displacement by the HRW provided by the inverse Prandtl shift. The neglected lower-order contributions to (4.1) consist of eigensolutions of the linearised NS operator that exhibit asymptotic growth as $\bar{r} \rightarrow \infty$ so as to match the $O(\epsilon^{5/7})$ -term in (3.26) and higher-order terms apparent in the expansion of $\hat{\Psi}$, \hat{P} for $R \rightarrow 0$.

With $\Delta := \bar{r}^{-1} \partial_{\bar{r}}(\bar{r} \partial_{\bar{r}}) + \bar{r}^{-2} \partial_{\vartheta\vartheta}$ being the Laplacian, the leading-order NS problem

reads

$$\bar{\psi}_\vartheta(\bar{\psi}_\vartheta/\bar{r})_{\bar{r}} - \bar{\psi}_\bar{r}^2 - \bar{\psi}_{\bar{r}}\bar{\psi}_{\vartheta\vartheta}/\bar{r} = -\bar{r}\bar{p}_{\bar{r}} + \bar{\Delta}\bar{\psi}_\vartheta, \quad (4.3a)$$

$$\bar{\psi}_{\bar{r}}\bar{\psi}_{\bar{r}\vartheta} - (\bar{r}\bar{\psi}_{\bar{r}})_{\bar{r}}\bar{\psi}_\vartheta/\bar{r} = -\bar{p}_\vartheta - \bar{r}(\bar{\Delta}\bar{\psi})_{\bar{r}}, \quad (4.3b)$$

supplemented with (2.3c–e) when evaluated for $\bar{y} = \vartheta = 0$,

$$\vartheta = 0: \quad \bar{\psi} = 0, \quad \bar{\psi}_{\vartheta\vartheta} = 0, \quad 2(\bar{\psi}_\vartheta/\bar{r})_{\bar{r}} + \bar{p} = \tau\bar{h}'', \quad (4.3c)$$

$$\vartheta = \pi: \quad \bar{\psi} = \bar{\psi}_\vartheta = 0. \quad (4.3d)$$

Matching ψ and p in the NS and the surrounding inner Rayleigh region, i.e. (4.1) and (3.26), completes the problem (4.3) governing $\bar{\psi}$, \bar{p} and \bar{h} . We have for

$$\bar{r} \rightarrow \infty: \quad \bar{\psi} \sim (\Lambda_0/2)(\bar{r} \sin \vartheta)^2 + o(\bar{r}) \quad (\vartheta \gg \bar{r}^{-2/3}, \quad \pi - \vartheta \gg \bar{r}^{-2/3}), \quad \bar{p} \rightarrow 0. \quad (4.3e)$$

The smallness of the remainder term imposed on $\bar{\psi}$ provides the required second kinematic far-field BC. Since we are dealing with the full NS equations, (4.3) already captures the inner Rayleigh region and its subregions upstream (SL) and downstream (HRW, $\bar{y} \sim \bar{r}\vartheta = O(\bar{r}^{1/3})$ there) of detachment; cf. figure 4(d). That is, (4.3e) implies already $(\bar{\psi}, \bar{p}) = O(\bar{r}^{2/3})$ and $\bar{h} = O(\bar{r}^{8/3})$ at the onset of the HRW. The BCs for $\vartheta = 0$ in (4.3c) describe zero tangential stress along and the net normal-stress jump across the detached streamline. Eventually, eliminating \bar{p} from (4.3a,b) yields the vorticity transport equation

$$(\bar{\psi}_\vartheta \partial_{\bar{r}} - \bar{\psi}_{\bar{r}} \partial_\vartheta)\bar{\Delta}\bar{\psi} = \bar{r}\bar{\Delta}^2\bar{\psi}, \quad (4.4)$$

to be solved subject to the first two BCs in (4.3c) and (4.3d,e). Hence, $\bar{\psi}$ is solely induced and parametrised by the externally exerted shear rate Λ_0 .

The variation of \bar{h} with \bar{r} is then found from integrating the capillary normal-stress jump in (4.3c) and, given the identical match of \bar{h} and H_- according to (3.1), two ICs to be imposed as $\bar{r} \rightarrow 0$. Before tackling their determination, one is first committed to capture the flow topology near detachment solely based on the information extracted from the NS problem posed above in the limit $\bar{r} \rightarrow 0$. The importance of this insight by far outweighs the perspective of obtaining the full numerical solution. Therefore, we have refrained from tackling this considerable challenge. (The considerations below suggest spectral collocation in the ϑ -direction as the method of choice.)

4.2. Flow close to detachment

As $\bar{\psi}$ must satisfy four BCs in (4.3c,d), the viscous terms are retained in the limiting forms of (4.3a,b) as $\bar{r} \rightarrow 0$ and $\vartheta \in [0, \pi]$. Requiring strict forward flow in the immediate vicinity of detachment,

$$\bar{\psi} > 0 \quad (\bar{r} \rightarrow 0), \quad (4.5)$$

is initially seen as a natural additional constraint. It is supported by the extensive numerical investigation by Kistler & Scriven (1994) of the full NS problem for a flow passing a wedge-shaped lip, see figures 2(b) and 4(f): this predicts an eddy at its underside in some situations associated with rather low to moderate Reynolds numbers but strictly forward flow detaching at its tip in the present high-Reynolds-number limit. The subsequent analysis demonstrates, however, that (4.5) is only met in the least singular situation singled out from the initial alternative ones.

4.2.1. The full inertial–viscous limit

The convective–viscous balance in (4.4) is restored in full if $\bar{\psi}$ varies essentially with $\ln \bar{r}$:

$$\bar{\psi} \sim \bar{g}(\vartheta) - \Gamma \ln \bar{r}/(2\pi) \quad (\bar{r} \rightarrow 0), \quad \Gamma \bar{g}'''/(2\pi) - 2\bar{g}'\bar{g}'' = (4\bar{g} + \bar{g}'')'. \quad (4.6)$$

We are hence concerned with a spiralling extension of a special type of a radial Jeffery–Hamel (JH) flow described by $\bar{g}(\vartheta)$ (see [Fraenkel 1962](#)), exhibiting the vorticity $-\bar{\Delta}\bar{\psi} = -\bar{g}''/\bar{r}^2$ and an outwards flow speed $\bar{g}'(\vartheta)/\bar{r}$ as collapsing in a line source of strength $\bar{g}'(\vartheta)$, due to a superimposed potential vortex of some strength Γ . Here the homogeneous BCs $\bar{g}(0) = \bar{g}''(0) = \bar{g}(\pi) = \bar{g}'(\pi) = 0$ originating in (4.3c,d) require $\Gamma = 0$, and \bar{g} represents an eigensolution of the full NS problem. Nevertheless, the case $\Gamma \neq 0$ and $\bar{g}'' \neq 0$, apparently unprecedented so far, might be of interest in a different context. We also remark that for an inviscid flow, removing the Stokes operator in (4.6), $\bar{g}(\vartheta)$ varies sinusoidally in general but linearly in the case of a potential flow.

A preliminary analytical–numerical study shows that there exist two eigensolutions \bar{g} . Each describes a distinctly different canonical flow topology as both exhibit a dividing streamline $\bar{g} = 0$ for $\vartheta = \vartheta_0 \simeq 1.12777$ and thus violate the premise (4.5) and point to the existence of a closed reversed-flow eddy. This is located either adjacent to the plate ($\bar{g} < 0$ for $\vartheta_0 < \vartheta < \pi$) or fully detached as bounded by the free streamline ($\bar{g} < 0$ for $0 < \vartheta < \vartheta_0$): see figure 8(a). In the first case, the flow undergoes pre-separation to reattach in the origin $\bar{r} = 0$; in the second, the free streamline attaches rather than detaches there from the plate. These flow pictures are the immediate consequence of including azimuthal higher-order corrections to the purely radial JH flow and extending the streamline pattern over the full NS scales: see figure 8(b). However, our scrutiny of the related literature does not disclose a clue to what, at first sight, is a rather pathological situation. In particular, the conception of a detached eddy with a stagnation point forming at the free and material streamline, to which the fluid particles stay attached, raises serious concerns.

We therefore rule out the JH solution as the local limit of the full NS solution. Notwithstanding its apparent shortcoming, however, we refer the interested reader to the higher-order corrections and some of the further impact of this limit in appendix §D. These findings are not required for the core arguments at present but potentially of interest for pursuing the study of this flow structure in a related context.

4.2.2. Alternative: extended Stokes limit

Discarding the possibility of a full inner NS problem, (4.6), leaves us with the degenerate situation of the dominant Stokes balances

$$0 \sim \bar{\Delta}^2 \bar{\psi}, \quad \bar{p}_{\bar{r}} \sim \bar{\Delta} \bar{\psi}_{,\vartheta} / \bar{r}, \quad \bar{p}_{,\vartheta} \sim -\bar{r} (\bar{\Delta} \bar{\psi})_{,\bar{r}} \quad (4.7)$$

and $\bar{\psi} \rightarrow 0$ as the origin $\bar{r} = 0$ is approached along any path from within the flow. We then expand $\bar{\psi}$ into the eigensolutions $\bar{\psi}_i$ of the biharmonic operator in (4.7) when supplemented with the homogeneous BCs in (4.3c,d) found by separation into the polar variables, following [Moffatt \(1964\)](#) and the references therein:

$$\bar{\psi} \sim \sum_{i=0}^{\infty} \bar{\psi}_i + O(\bar{r}^{\sigma_n + \sigma_q}) + c.c., \quad \bar{\psi}_i := \bar{r}^{\sigma_i} f_i(\vartheta), \quad \text{Re } \sigma_{i+1} > \text{Re } \sigma_i > 0. \quad (4.8)$$

Herein, σ_i denotes the i -th eigenvalue, f_i the corresponding eigenfunction of the azimuthal variation, and the remainder term arises from the dominant contribution to the quadratic inertial terms in (4.4), not captured by the Stokes balance and of $O(\bar{r}^{\sigma_n + \sigma_q - 3})$. Therefore, n and q stand for the lowest indices i such that f_n, f_q are both non-trivial and their coupling produces a non-trivial inhomogeneity.

Expansion (4.8) casts the biharmonic problem into the series of eigenvalue problems

$$\mathcal{S}_i \{f_i\} = f_i(0) = f_i''(0) = f_i(\pi) = f_i'(\pi) = 0, \quad (4.9a)$$

$$\mathcal{S}_i \{Q\} := [(\sigma_i - 2)^2 + \text{d}^2/\text{d}\vartheta^2] (\sigma_i^2 + \text{d}^2/\text{d}\vartheta^2) \{Q\} \quad (4.9b)$$

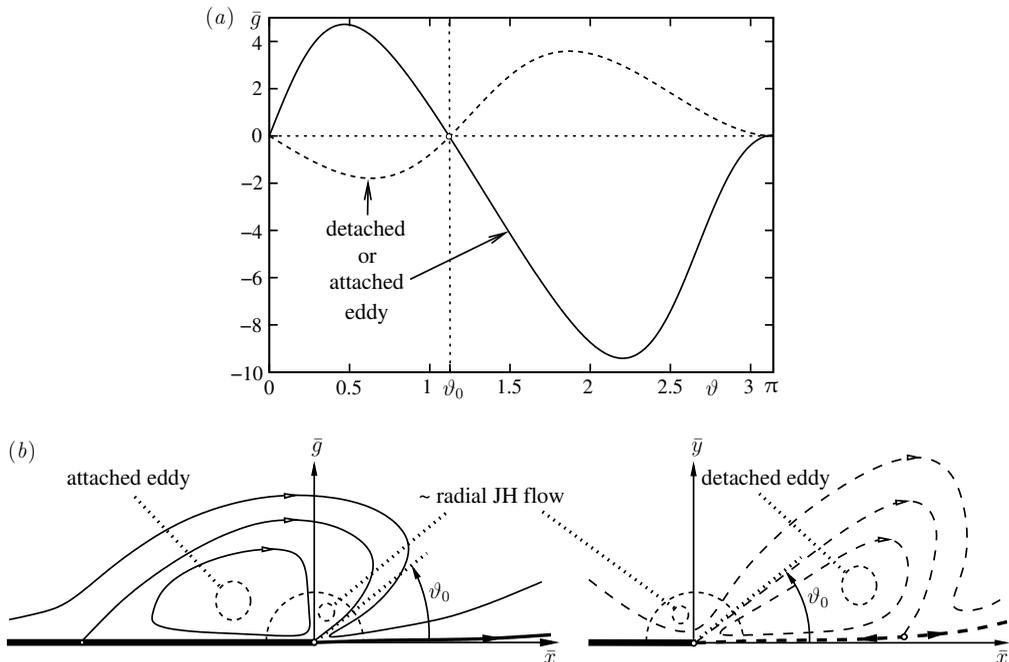


FIGURE 8. (a) Eigensolutions of (4.4) referring to a JH flow given by (4.6); (b) sketched flow patterns for the two cases in (a): reversed-flow bubble upstream of detachment or dictating attachment of free streamline.

for any function Q . The reduced Stokes operator \mathcal{S}_i acting on ϑ and parametrised by the discrete eigenvalues is already seen in (4.6) as this replaces (4.8) for $\sigma_i = 0$. One readily finds that (4.9) has no solution in the degenerate cases $\sigma_i = 1$ and $\sigma_i = 2$. In any other case, the first two BCs in (4.9a) yield

$$f_i = a_i \sin(\sigma_i \vartheta) + b_i \sin[(\sigma_i - 2)\vartheta], \quad (4.10a)$$

where the constants a_i and b_i , as functions of Λ_0 to be determined by the global solution to (4.3), must not all be zero. Notably, the $\sin(\sigma_i \vartheta)$ -term refers to a potential-flow contribution. The eigenvalue relation $\sin(2\sigma_i \pi) = 0$ equivalent to the last two BCs enforces

$$\sigma_i = (1 + i)/2. \quad (4.10b)$$

In turn, (4.10a) holds for some real a_i and b_i satisfying

$$b_i = -a_i \quad (i = 0, 2, 4, \dots), \quad (2 - \sigma_i)b_i = \sigma_i a_i \quad (i = 1, 3, 5, \dots), \quad (4.10c)$$

which confirms that $f_1 \equiv f_3 \equiv 0$ and $a_2 f_0 \equiv a_0 f_2$ and, a posteriori, the validity of (4.8): see appendix §E. As σ_i take on integer values for i being odd, it is readily seen that exactly this category refers to regular eigensolutions $\bar{\psi}_i$. Their series, ordered by ascending integer powers in \bar{x} and \bar{y} ,

$$\bar{\psi}_5 = -4a_5 \bar{y}^3, \quad \bar{\psi}_7 = -8a_7 \bar{x} \bar{y}^3, \quad \bar{\psi}_9 = 40a_9 \bar{y}^3 (\bar{y}^2/15 - \bar{x}^2/3), \quad \dots, \quad (4.11)$$

ensues systematically from expressing $\bar{\Delta}^2$ accordingly and using the BCs. We also infer from (4.7), (4.9) and (4.10a) that

$$\bar{p} - \bar{p}_0 \sim \sum_{i=0, i \neq 3}^{\infty} \bar{r}^{\sigma_i - 2} p_i(\vartheta) + O(\bar{r}^{\sigma_n + \sigma_q - 2}), \quad p_i = 4b_i(\sigma_i - 1) \cos[(\sigma_i - 2)\vartheta]. \quad (4.12)$$

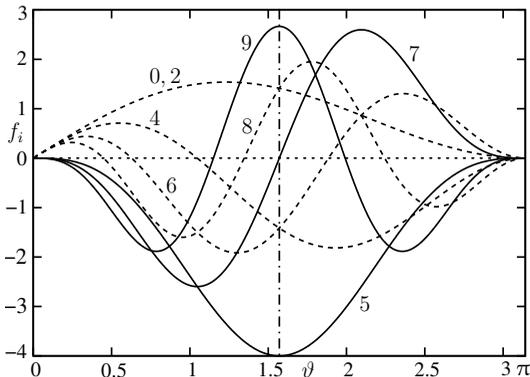


FIGURE 9. Eigenfunctions f_i of Stokes operator and their symmetry properties, see (4.10): $a_i = 1$, labels indicate $i = 0, 2, 4, 6, 8$ (solid), $i = 5, 7, 9$ (dashed).

The constant offset pressure \bar{p}_0 is part of the solution to the full NS problem.

The symmetry of f_i in i around $i = 1$ and its azimuthal symmetry/antisymmetry with respect to $\vartheta = \pi/2$ for odd/even values of σ_i (i.e. odd values of i) deserve a comment. The first eight members of the series f_i with a_i set to unity are plotted in figure 9. One then finds that $f_0 \geq 0$, $f_5 \leq 0$, and $f_i(\vartheta)$ changes its sign $(i-2)/2$ times if $i = 4, 6, \dots$ and $(i-5)/2$ times if $i = 7, 9, \dots$ over the interval $(0, \pi)$. Therefore, exactly three alternatives accommodate the forward-flow condition (4.5):

- (A) $a_0 > 0$;
- (B) $a_0 = 0$ and $a_2 > 0$;
- (C) $a_0 = a_2 = a_4 = 0$ and $a_5 < 0$.

We conveniently restate (4.8) in general more precisely as

$$\bar{\psi} \sim \sum_{i=0}^{\infty} \bar{r}^{\sigma_i} g_i(\vartheta), \quad g_0 := f_0, \quad (4.13)$$

where the functions g_i represent the solutions to the hierarchy of inhomogeneous Stokes problems provoked by the inertia terms in (4.4), which cause the remainder term in (4.8). As we now demonstrate, the forcing of these eigensolutions of the Stokes operator by the higher-order, convective terms controls the selection of the leading non-zero coefficient a_i of the homogeneous contribution f_i to g_i . Substituting (4.13) into (4.4) and collecting powers of \bar{r} results in the inhomogeneous extension of (4.9) for $i > 0$:

$$\mathcal{S}_i\{g_i\} = I_i(\vartheta) := \sum_{j=0}^{i-1} I_{i,j}(\vartheta), \quad (4.14a)$$

$$I_{i,j}(\vartheta) := [(\sigma_j - 2)g'_k - \sigma_k g_k \, d/d\vartheta](\sigma_j^2 g_j + g''_j), \quad k := i - j - 1, \quad (4.14b)$$

$$g_i(0) = g''_i(0) = g_i(\pi) = g'_i(\pi) = 0, \quad (4.14c)$$

where (4.14b) complies with the identity $\sigma_j + \sigma_k \equiv \sigma_{j+k+1}$, see (4.10b). The self-adjointness of the homogeneous Stokes operator defined by (4.9) gives

$$0 = \int_0^\pi \mathcal{S}_i\{g_i\} f_i(\vartheta) \, d\vartheta = S_i := \int_0^\pi I_i(\vartheta) f_i(\vartheta) \, d\vartheta. \quad (4.15)$$

This describes the well-known three alternatives: the solution of (4.14) is unique if $f_i \equiv 0$; it is non-unique if f_i is non-trivial and $S_i = 0$; it does not exist otherwise. Thus (4.15) establishes the following analysis of the possible cases concerning the solvability of (4.14).

Case: $a_0 \neq 0$. In this least-degenerate scenario including case (A) above, (4.13) is

specified as $\bar{\psi} \sim \bar{r}^{1/2} f_0 + \bar{r} g_1 + \bar{r}^{3/2} g_2 + O(\bar{r}^2)$; (4.10) gives $f_0 = a_0[\sin(\vartheta/2) + \sin(3\vartheta/2)]$ and (4.14b) $I_1 = 3a_0^2[\sin(2\vartheta)/2 + \sin(3\vartheta)]$. Since $f_1 \equiv 0$, we construct for $i = 1$ the unique solution $g_1 = a_0^2[37\sin(\vartheta) + 32\sin(2\vartheta) + 9\sin(3\vartheta)]/192$ of (4.14). In turn, we specify (4.14) and (4.15) for $i = 2$. A tedious but straightforward calculation involving g_1 and $f_2 \equiv a_2 f_0/a_0$ yields $S_2 = -25\pi a_0^2 a_2/128$ so that g_2 does not exist. We are thus left with the following less singular situation.

Case: $a_i = 0$ ($0 \leq i < n$), $a_n \neq 0$. Here n identifies the index of the dominant non-trivial eigensolution so that $g_n = f_n$. Accordingly, (4.14b) produces non-trivial $I_{i,j}$ for $j, k \geq n$ only. This confirms that $I_i \equiv 0$ ($0 \leq i \leq 2n$) as the self-coupling of f_n yields the potential lowest-order inhomogeneity

$$I_{2n+1} = I_{2n+1,n} = -4b_n(\sigma_n - 1)(\sigma_n - 2)\{a_n\sigma_n \sin(2\vartheta) + b_n \sin[(2\sigma_n - 4)\vartheta]\}, \quad (4.16)$$

which conforms to the case $n = q$ in (4.8). It is emphasised that I_{2n+1} vanishes identically only for $n = 1$ ($\sigma_1 = 1$), $n = 3$ ($\sigma_3 = 2$) and $n = 5$ ($\sigma_5 = 3$). Furthermore, (4.15) gives after some standard manipulations, involving σ_n and σ_{2n+1} specified by (4.10b),

$$S_{2n+1} = \begin{cases} 0 & (n \neq 2), \\ 3\pi a_2^2 a_5/2 & (n = 2). \end{cases} \quad (4.17)$$

The last statement requires $a_2 = 0$. This renders the forward-flow case (B) also not possible. Hence, the scenario (C) motivates the following discussion of the special case $n = 5$.

Case: $a_i = 0$ ($0 \leq i < 5$), $a_5 \neq 0$. The result (4.17) includes that the here dominant eigensolution of the Stokes operator $\bar{\psi}_5$ given by (4.11), describing a non-degenerate flow profile at separation, trivially generates a vanishing inhomogeneity I_{11} . That said, (4.13) then degenerates and reads more accurately, with the help of (4.10b),

$$\bar{\psi} \sim \bar{\psi}_5 + \sum_{i=q}^{\infty} \bar{r}^{(1+i)/2} f_i + \bar{r}^{(7+q)/2} g_{6+q} + o(\bar{r}^{(7+q)/2}) \quad (q > 5, a_q \neq 0). \quad (4.18)$$

At first, any index $q > 5$ is conceivable. If (4.18) initiates the solution to the full NS problem, such an index indicating the non-trivial follow-up term to $\bar{r}^3 f_5$ must exist. As a central observation, the lowest-order inhomogeneity in (4.14a) specified by (4.14b) is $I_{6+q} = I_{6+q,5} + I_{6+q,q}$ and produces g_{6+q} , where the eigenfunction f_{6+q} corresponds to the eigenvalue $\sigma_{q+6} = (7+q)/2$. Inserting these findings into (4.15) yields indeed $S_{6+q} \equiv 0$ as for (4.17) but for any q , where we skip the technical details. This guarantees the existences of g_{q+6} and, in turn, of (4.18).

As an important step, the above analysis determines the least singular (most-degenerate) local representation of $\bar{\psi}$ to be given by case (C) extended by (4.18) as the sole reliable option satisfying (4.5). It shall be emphasised that the impact of the interactive flow on flow detachment on the NS scales is condensed into the aforementioned (pending) dependence of the coefficient a_5 on A_0 .

The shear rate at the plate immediately upstream of detachment observed on the global scale reads $u_y|_{y=0} \sim \bar{\psi}_{,\vartheta\vartheta}(\bar{r}, \pi)/\bar{r}^2$, according to (4.1) and (4.3d). Since (4.10) entails $f_i''(\pi) = 0$ for odd i , cf. (4.11), and $f_i''(\pi) = 2a_i(-1)^{i/2}(1-i)$ for even i , it is dominantly fixed either by the eigenfunction f_j of the smallest even index, $j \geq 6$, that enters (4.18) or g_{6+q} . With dots abbreviating smaller terms, that shear rate tends to zero at detachment in the form

$$u_y|_{y=0} \sim 2a_j(-1)^{j/2}(1-j)(-\bar{x})^{(j-1)/2} + (-\bar{x})^{(3+q)/2} g_{6+q}''(\pi) + \dots \quad (\bar{x} \rightarrow 0-). \quad (4.19)$$

Since (4.5) requires $u_y|_{y=0} > 0$ here, we expect either $a_j > 0$ ($a_j < 0$) for $j = 6, 10, 14, \dots$ ($j = 8, 12, 16, \dots$) or $f_{6+q}''(\pi)$ behaves such that $g_{6+q}''(\pi) > 0$. Typically, the adverse

pressure gradient predicted by (4.12) in the form $\bar{p} - \bar{p}_0 \sim -24a_5\bar{x} + O(\bar{r}^{(q-3)/2})$ initiates flow detachment. Downstream of this, (4.3d) finally predicts the regular approximation

$$\bar{h} \sim \bar{h}(0) + \bar{h}'(0)\bar{x} + \bar{p}_0\bar{x}^2/(2\tau) - 4a_5\bar{x}^3/\tau \quad (\bar{x} \rightarrow 0+). \quad (4.20)$$

Let us first indicate how to fix $\bar{h}(0)$ and $\bar{h}'(0)$ and complete the analysis right at this stage, i.e. without taking into consideration any smaller length scale.

As an obvious geometrical requirement, $\bar{h}(0) = 0$ then. In full agreement with the current status of the theory, the position of flow detachment not only defines the origin $x = y = 0$ but an arbitrary point of the upper side of the plate rather than it necessarily coincides with the trailing edge, as a genuine geometrical constraint. Detachment further upstream then requires the actual static wetting or contact angle, observed in the NS region, as a novel input quantity being so close to π that it is approximated by $\pi - \epsilon^{3/2}\bar{h}'(0)$. This determines a positive value of $\bar{h}'(0)$. However, and as an immediate consequence of the slenderness of the lower free streamline, this thereby introduced distinguished limit refers to the quite exceptional break-away of an almost perfectly hydrophobic liquid. Additionally, such a scenario demands for the geometrical constraint $\bar{h} > 0$ for $\bar{x} > 0$, which admittedly cannot be guaranteed as long as the numerical solution of the above NS problem is not available. It is also not likely to occur in reality, where unavoidable (though here neglected) surface imperfections already affect the flow described on the vertical NS scale. It is a natural step, therefore, to seek the location of flow detachment indeed at the trailing edge. However, then $\bar{h}'(0)$ remains undetermined as long as its microscopic shape remains unresolved.

The outcome of these considerations is threefold. Firstly, we expect both $\bar{h}(0)$ and $\bar{h}'(0)$ fixed by conditions of matching the full NS and a Stokes flow in a hidden region of an extent much smaller than that of the encompassing NS region. Secondly, as we raised in the introduction to §4, the description of that creeping flow must take into account the meniscus formed by the actual slope of the free streamline at its detachment point of three-phase contact as a hitherto unconsidered physical input. And third, that new length scale must resolve the microscopic contour of the plate with sufficient accuracy.

4.3. Distinguished Stokes limits and wetting properties

Albeit possibly not satisfied in a realisation of the flow, let us treat the surface of the plate as locally chemically heterogeneous and ignore distributed roughness on all scales for the sake of clarity. Then the so-called quasi-static apparent contact angle, β , is observed between the wetted plate and the tangent to the free streamline at its point of detachment and formation, where three phases (locally) at rest meet under the Young–Dupré equilibrium: for its precise conceptual foundation we refer to Teletzke, Davis & Scriven (1988), Kistler & Scriven (1994), Whyman, Bormashenko & Stein (2008) and Bonn *et al.* (2009). Since this macroscopic contact angle summarises all related submicroscopic phenomena (see Kistler & Scriven 1994, and references therein) and shall apply even to the smallest scales identified in the flow, we have consistently used the notion “microscopic” in the context with the resolved geometry of the trailing edge.

To progress further, we introduce the new length scale $\ell \ll \epsilon^{1/2}$, non-dimensional with the nominal film thickness \tilde{H} . In the new flow region, $[\hat{x}, \hat{y}] := [x/(\epsilon\ell), y/\ell]$ and $\hat{r} := r/\ell = (\hat{x}^2 + \hat{y}^2)^{1/2}$, see (3.18), are of $O(1)$ as $\ell \rightarrow 0$. Hence, supplementing (4.1) with (4.18), the associated increase of $\bar{p} - \bar{p}_0$ and (4.20) suggests the two-parametric expansion

$$\left[\frac{\psi}{\ell^3 \epsilon^{-1/2}}, \frac{p - p_- + gy - \epsilon\bar{p}_0}{\ell \epsilon^{1/2}}, \frac{h_-}{\ell} \right] \sim \left[\hat{\psi}(\hat{x}, \hat{y}), \hat{p}(\hat{x}, \hat{y}), \hat{h}_0(\hat{x}) + \frac{\ell}{\epsilon^{1/2}} \hat{h}_1(\hat{x}) \right]. \quad (4.21)$$

The $O(1)$ -quantities $\hat{\psi}$, \hat{p} , \hat{h}_0 and the only first-order correction of interest \hat{h}_1 are to be found. The scaled elevation $\hat{h}(\hat{x}) := h_-/\ell$ of the detaching streamline is determined by the capillary normal-stress jump in (2.3e). All terms on its left side are retained to leading order, and that becomes of $O(\ell\epsilon^{1/2})$. However, $\varkappa_- \sim \ell^{-1}\hat{h}''/(1+\hat{h}'^2)$, stating that the capillary number at play, $\ell^2\epsilon^{1/2}/\tau$, is small. This is also inferred from reducing Ca in (2.2b) by the small relative velocity scale $\ell^2/\epsilon^{1/2}$. In turn, $\hat{h}'' \equiv 0$, and matching (4.21) and (4.20) shows that the lower free streamline remains horizontally inclined under an angle no larger than of $O(\alpha^{3/2})$:

$$\hat{h}_0 = \bar{h}(0)/\Delta, \quad \hat{h}_1 = \bar{h}'(0)(\hat{x} - \hat{x}_d)/\Delta. \quad (4.22)$$

Here the parameter Δ shall measure the strength of the required distinguished limit,

$$\ell = \Delta\epsilon^2, \quad 0 < \Delta = O(1), \quad (4.23)$$

and $(\hat{x}, \hat{y}) = (\hat{x}_d, \hat{h}_0)$ denote the position of the actual detachment point, \mathcal{D} , taken as known first.

Let Σ denote the resolved surface of the plate. Inspection of (2.3) and the behaviour (4.22) confirm that the leading-order quantities $\hat{\psi}$, \hat{p} satisfy

$$\hat{\Delta}^2\hat{\psi} = 0, \quad \hat{p}_{\hat{x}} = \hat{\Delta}\hat{\psi}_{\hat{y}}, \quad \hat{p}_{\hat{y}} = -\hat{\Delta}\hat{\psi}_{\hat{x}}, \quad \hat{\Delta} := \partial_{\hat{x}\hat{x}} + \partial_{\hat{y}\hat{y}}, \quad (4.24a)$$

subject to mixed boundary conditions in the limit of zero capillary number on

$$\hat{r} \rightarrow \infty: \quad \hat{\psi} \sim -4a_5\hat{y}^3 + o(\hat{r}^{5/2}), \quad (4.24b)$$

$$\text{on } \Sigma \ (\hat{x} < \hat{x}_d): \quad \hat{\psi} = \hat{\psi}_{\hat{y}} = 0, \quad (4.24c)$$

$$\hat{y} = \hat{h}_0 \ (\hat{x} \geq \hat{x}_d): \quad \hat{\psi} = \hat{\psi}_{\hat{y}\hat{y}} = 0. \quad (4.24d)$$

Once $\hat{\psi}$ is found, one can calculate \hat{p} by integration, giving $\hat{p} \sim -24a_5\hat{x} + O(1)$. This matches identically the small- \bar{r} form of p in §4.2.2 as the reminder term negotiates a constant of integration found from the $O(\epsilon^{3/2})$ -contribution to (4.1). In accordance with the above results and likewise, the neglected remainder term in (4.24b) expresses the second necessary far-field condition and the absence of an eigensolution of the NS problem of $O(\epsilon^{3/4})$ that would enter the right-hand side of (4.1). This seems to be a natural choice, as (3.26) would require it to die out for large values of \hat{r} . Rather, (4.24d) enforces an $O(1)$ -correction $a_5\hat{g}(\vartheta)$, say, in the large- \hat{r} form of $\hat{\psi}$. This is governed by $\mathcal{S}_{-1}\hat{g} = 0$, cf. (4.9b), subject to $\hat{g}(0) = -4a_5\hat{h}_0^3$, $\hat{g}''(0) = -24a_5\hat{h}_0$, $\hat{g}(\pi) = \hat{g}'(\pi) = 0$. Eventually,

$$\hat{\psi}/a_5 \sim -4\hat{y}^3 \cdots + \hat{g}(\vartheta) + o(1), \quad \hat{g} := -6\hat{h}_0(\sin \vartheta)^2 - 4\hat{h}_0^3[1 + \sin(2\vartheta)/(2\pi) - \vartheta/\pi], \quad (4.25)$$

where the dots indicate potential eigensolutions of $o(\hat{r}^2)$. The behavior (4.25) provides the match of (4.21) with (4.1) supplemented with an $O(\epsilon^{9/2})$ -contribution, hence also excited by the displacement (4.2) of the interface. While that of $O(\epsilon^{3/2})$ is controlled by the linearisation of $\bar{\psi}$ as $\bar{y} \rightarrow 0$, this is due to the corresponding third-order terms. As these dominate as $\bar{r} \rightarrow 0$ where $\bar{\psi} \sim 4a_5\bar{y}^3$, evaluating \hat{g} for $\vartheta \rightarrow 0$ describes the feedback of the displacement on the flow near detachment.

The case of a perfectly flat surface associated with $\hat{h}_0 \equiv 0$ and the trivial solution $\hat{\psi} = -4a_5\hat{y}^3$ recovers the dominant Stokes limit of the full NS solution for $\bar{r} \rightarrow 0$ and the aforementioned pathological case of fully hydrophobic dewetting; both x_d and ℓ remain unspecified then. This situation is therefore ruled out, and we are indeed left with flow detachment in a vicinity of the originally sharp plate edge covered by the Stokes region, where the microscopic resolution of the edge dictates the definition of ℓ . We henceforth

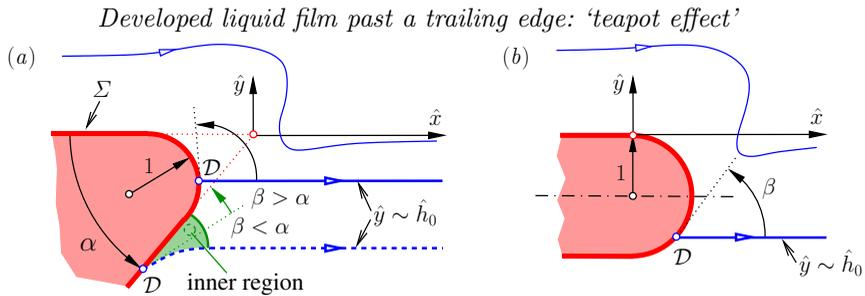


FIGURE 10. Stokes flow around resolved smoothed trailing edge: (a) wedge-type ($\alpha > 0$), inner region emerging for $\beta < \alpha$ (green); (b) plate-type and semi-circular ($\alpha = 0$), no inner region.

refer to the sketch of the flow around the resolved edge in figure 10, detailing figures 2(b) and 4(f) on the new scale for various values of β . The edge is, without substantial loss of generality, assumed to be given by a smoothed but at first ideal wedge of cut-back angle α and with an apex lying in the origin of coordinates. Then the curvature radius typical of the rounded nose advantageously defines ℓ ; the degenerate situation of a wedge still found sharp when viewed on the scale ϵ^2 is assumed in the limit $\Delta \rightarrow 0$. The case of specific relevance $\alpha = 0$ can be interpreted as a plate-type thin tip formed by a semi-circle and of local thickness 2ℓ (figure 10b).

Assuming $\Delta = 1$ in (4.23) and $\tilde{H} = 1$ mm (table 1) typically gives a quite small physical scale $\ell\tilde{H} \simeq 0.01\text{--}0.04$ μm . However, it is large enough to consider the asymptotic theory applicable to curvature radii achieved by manufacturing practice.

Completing our flow model at this stage is indeed possible for a non-degenerate, smoothed wedge tip and a sufficiently large apparent wetting angle β as the wedge geometry imposes a closure condition on (4.24). This fixes the location of \mathcal{D}

$$\text{on } \Sigma: \quad d\hat{y}/d\hat{x} \sim \tan \beta + o(\epsilon^{3/2}). \quad (4.26)$$

This describes the general, non-degenerate case where $\bar{h}(0)$ is found by virtue of (4.22). Evidently, then also $\hat{h}'(0) = 0$ as the linear follow-up problem to (4.24) governing disturbances of $O(\ell/\epsilon^{1/2})$ in (4.21) has the trivial solution. Higher-order perturbations, already affected by the curvature of the detaches streamline, control the (physically insignificant) remainder term in (4.26). Proceeding in this manner determines successively the two initial conditions that each term arising in the expansion of h_- in (4.1) has to meet as $\bar{r} \rightarrow 0$. This consideration confirms self-consistency of the proposed theoretical framework. As a crucial result, the flow wets the underside of the wedge as \hat{h}_0 represents a (strictly) monotonic function of β , which decreases from 0 as β decreases from π . This justifies our reference to the teapot effect. The pathological limit $\beta \rightarrow \pi^-$ or $(\hat{x}_d, \hat{h}_0) \rightarrow (0, 0)$, however, puts a non-trivial value of $\hat{h}'(0)$ in the focus. We only note that the above analysis by inspection gives $\ell = O(\epsilon)$ in the degenerate case $\bar{h}(0) = 0$, $\bar{h}'(0) > 0$. On the other extreme, \mathcal{D} has reached the point on the nose where its curvature vanishes once β has become as small as α . All together, we arrive at the geometrical constraint

$$\pi - \epsilon^{3/2}\bar{h}'(0) \geq \beta \geq \alpha. \quad (4.27)$$

The variation of \hat{h}_0 with β is more and more squeezed towards the edge as this gets sharpened. Finally, \mathcal{D} is seen as *pinned* to the edge as (4.27) is interpreted as the well-known Gibbs inequality: see Oliver, Huh & Mason (1977); Dyson (1988); Kistler & Scriven (1994). In accordance with the last authors, we find that the distance of \mathcal{D} from the apex decreases with both increasing values of β and the Reynolds number.

The formidable task of solving the Stokes problem (4.24), parametrised by α and β , has

not been accomplished yet. Most importantly, in the situation sketched in figure 10(b), mastering this challenge will establish a comprehensive flow description in the entire range $\pi > \beta > 0$ of physical significance. If, however, $\beta \geq \alpha$, determining the actual position of \mathcal{D} requires the introduction of a further, inner Stokes region, as indicated in figure 10(a). Contrasting with its counterpart (4.24), there the governing problem is of non-degenerate free-surface type, thus controlled by a capillary number of $O(1)$, to accommodate to the necessary local bending of the detaching streamline. We expect \mathcal{D} to wander the further away from the apex the smaller β is, with its position fixed by a constraint arising of the interplay of these staggered Stokes regions. This is a topic of our future activities.

As the final step, we focus on the flow properties in the immediate vicinity of detachment, specified on condition (4.27). Here we again follow Moffatt (1964) in his analysis of local eigensolutions of (4.24) varying algebraically with distance from a singular point at a rigid wall. These suggest that the streamlines are locally pushed away from the nose. Moffatt (1964, §3.2) also showed that a related class of eigensolutions controls the behaviour of $\hat{\psi}$ at small distances $\hat{d} = [(\hat{x} - \hat{x}_d)^2 + (\hat{y} - \hat{h}_0)^2]^{1/2}$ from the detachment point: using (4.24a,c,d) and reusing the azimuthal angle, $\vartheta := \arctan[(\hat{y} - \hat{h}_0)/(\hat{x} - \hat{x}_d)]$, yields for $0 \leq \vartheta \leq \beta$ and

$$\hat{d} \rightarrow 0: \frac{\hat{\psi}}{\hat{a}\hat{d}^\sigma} \sim \begin{cases} \sin(\sigma\vartheta) \sin[(\sigma - 2)\beta] - \sin(\sigma\beta) \sin[(\sigma - 2)\vartheta] + c.c. & (\sigma \neq 2), \\ \sin(2\vartheta) - \vartheta/\beta & (\sigma = 2). \end{cases} \quad (4.28)$$

The constant \hat{a} is determined by the full solution to (4.24), and σ appears to be a (complex) eigenvalue related to β by

$$(\sigma - 1) \sin(2\beta) = \sin[2\beta(\sigma - 1)] \quad (\sigma \neq 2), \quad \tan(2\beta) = 2\beta \quad (\sigma = 2). \quad (4.29)$$

A continuous relationship requires $\beta = 3\pi/4$ for $\sigma = 2$. One readily confirms that the eigensolutions considered in §4.2.2 are recovered in the limit $\beta \rightarrow \pi$. Equation (4.29) is symmetric with respect to $\text{Re } \sigma - 1$. However, physically admissible solutions require the flow speed, of $O(\hat{d}^{\sigma-1})$, to vanish and the shear and the normal stress (the pressure), both of $O(\hat{d}^{\sigma-2})$, on Σ being integrable as $\hat{d} \rightarrow 0$ (and not to compromise the validity of the Young–Dupré equilibrium). Thus only values of σ having $\text{Re } \sigma > 1$ are permitted, anticipated by the requirement $\hat{\psi} = 0$ at detachment in (4.24d). The plot of the real branches of (4.29) in figure 11 illustrates the infinite multiplicity of σ , not considered by Moffatt (1964), the asymptotes $\beta \rightarrow \pi/2, \pi$ as $\text{Re } \sigma \rightarrow \infty$ and the local extrema of β . There (4.29) is continued to complex values of σ , via (4.28) associated with Moffatt’s (1964) exceptional infinite sequence of eddies. Hence, our flow model does not predict a single eddy as do the calculations by Kistler & Scriven (1994) for moderately large Reynolds numbers but this series of eddies if the value of β falls below its absolute minimum. Moffatt (1964) predicted this well-established threshold as $\simeq 78^\circ$; here we recomputed it as $\simeq 79.557^\circ$ for $\sigma \simeq 3.7818$.

A more elaborate discussion of these details and their consequences requires the yet pending full numerical solution of (4.24).

5. Conclusions and further perspectives

As a unexpected extension of the interactive flow structure around flow detachment at the free plate edge, we report neutral capillary Rayleigh modes on the upper free surface solely and immediately upstream of the edge. Demonstrating this confidently calls for solving a signalling problem where typically a compact forcing dividing the flow into an upstream and an downstream part. Here this is provided by a delta functional

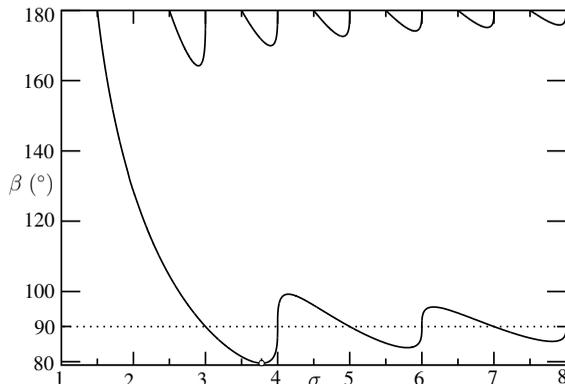


FIGURE 11. Contact angle β vs. real σ from (4.29) having absolute minimum (circle).

describing the transition of the vertical flow component over the geometric discontinuity formed by the trailing edge but tied in with an additional non-compact excitation by the displacement of the Hakkinen–Rott wake, necessary to provoke the non-trivial Rayleigh state.

The small-scale/small-amplitude ripples differ markedly in their origin from those already predicted by Bowles & Smith (1992) upstream of a wall-mounted obstacle over the interactive length scale. Accordingly, they are separated a streamwise extent of $O(\epsilon)$ from those of much larger wavelength found in the solutions of the interaction problem and set off by that wake in the downstream direction on both free surfaces in phase for $0 < T < 1/2$. On the other hand, since these rather long waves on the upper free surface are observed even upstream of the trailing edge for $T > 1$ (Scheichl *et al.* 2018), they collapse there with the short Rayleigh modes when $T \sim 1$, as the long-wave limit of the latter indicates (figure 6). This heralds how the introduction of a reduced streamwise length scale paves the way for an Euler stage to regularise the breakdown of viscous–inviscid interaction in a more general setting when the measure $T - 1$ of the typical counteracting dispersive effects, namely capillary versus convective streamline curvature, of classical Korteweg–de Vries-type changes sign. Albeit already spotted in related studies (Gajjar 1987; Bowles & Smith 1992; Kluwick *et al.* 2010), this has not been investigated in due detail. Having in mind the anomalous dispersion for classical linear capillary waves, we find it justifiable to speak of “choking” when both the wavelength and the amplitude of the capillary ripples, controlled by the dominant eigensolution $\psi'_0(y)$ of the Rayleigh operator and triggered by the displacement of the Hakkinen–Rott wake, diverge for $T \rightarrow 1-$. This consideration highlights the identical nature of the threshold $T = 1$ in this long-wave limit as for the interactive flow.

Neither the onset of the interactive, long waves above the plate for $T \rightarrow 1+$ nor the formulation of additional conditions imposed at the plate edge to account correctly for the upstream influence that render them unique have yet been clarified satisfactorily (cf. Scheichl *et al.* 2018). This and other exciting related phenomena attributed to the solution of the interaction problem downstream of the edge, such as its sound regularisation when $T - 1/2$ changes sign and attracting attention through (2.14*d–f*) and (2.17), are topics of our current research. A stability analysis of the detached interactive flow, where unsteadiness of the streamwise momentum balance becomes typically explicit in the lower deck, should clarify the analogy with the classical linear waves of Rayleigh–Plateau type.

As a major conclusion of our analysis, the layer undergoes its break-away from the

trailing edge at its downside when this is geometrically resolved in a least-degenerate but most simple manner as a (cut-back) wedge having a rounded nose. As a rule of thumb, the higher the wettability, the more the fluid “sticks” on the underside and the more the point of three-phase contact or detachment is remote from the plane wall on top. In the authors’ mind, the present analysis rationalises for the first time how a high-Reynolds-number flow negotiates the formation of free streamline with due rigour. As the vital idea, any physically viable flow always “feels” a small reference length (the nose radius ℓ) that resolves the abstraction of geometrical perfection (the sharp trailing edge). This then defines the smallest scales at play and hence controls the thereby arising Stokes limits and local dewetting or film rupture. As an interesting aspect, the convective influence and thus the flow profile stretching towards the upper free surface is only felt through a single coefficient of the dominant eigensolution of the Stokes operator. Pinpointing the flow on those smallest, geometrically induced length scales provides a self-consistent and qualitatively reasonable explanation of the teapot effect observed in the detachment of a high-momentum wall jet. The underlying continuum hypothesis is admissible as long as the smallest scales are so large that the liquid/gaseous interface can be taken as infinitely thin. Expectations are high that this appealing and promising conception stimulates future research in this direction.

The Stokes problems governing the steady free-surface flow on the smallest scales represent the central building block for completing the rigorous examination of the teapot effect. This appears as an essentially hydrodynamic phenomenon, but the adjustment of the flow to the three-phase equilibrium defining the wetting properties in terms of the apparent contact angle represents an essential ingredient. More will be able to be said and further progress sparked once the inner Stokes problem is established and the outstanding solutions of these core problems are available.

Last not least, we feel an urgent need for careful and systematic laboratory experiments, with the ultimate goal to corroborate the theoretical findings on all scales. Here the values in the tables 1 and 2 (§ 2.2) might be helpful.

Acknowledgements

Financial support from the Austrian Research Promotion Agency (FFG, grant no.: 849109, COMET K2 program: *XTribology*) and from a UCL Mathematics Teaching Assistantship is greatly acknowledged. The authors express their thanks to Dr. S. N. Timoshin (Department of Mathematics, UCL) for fruitful discussions and helpful comments.

Declaration of interest

The authors report no conflict of interests.

Appendix A. Hakkinen–Rott wake: higher-order scheme

To elucidate the structure of (3.2) and (3.5), we have to match the latter to the appropriate expansion

$$F := \Psi / (\Lambda_0^{1/3} X^{2/3}) \sim f_{\text{HR}}(\eta) + c_1 \Lambda_0^{-4/3} X^{1/3} [\ln X F_1(\eta) + F_2(\eta)] + O(X^{2/3} (\ln X)^2) \quad (\text{A } 1)$$

for $\eta = O(1)$ as $X \rightarrow 0+$ and with $F_{1,2}$ to be found. The logarithmic contributions to (3.2)–(A 1), by anticipating $c_{1,2} \neq 0$, comply with the representation

$$\Psi \sim \Lambda_0 Z^2 / 2 + P(0-) Z^3 / 6 + (P - P_-) [\Lambda_0^{-1} + P'(0-) \Lambda_0^{-2} Z \ln Z + O(Z)] \quad (\text{A } 2)$$

of (3.5), found with the help of (2.16), in the overlap $1 \gg Z \gg X^{1/3}$ or $X^{-1/3} \gg \eta \gg 1$, see (3.1), with the expansion (A1). There they cause a reordering of its terms arising for large values of η , as seen from expressing Z in (A2) in terms of η :

$$F \sim \frac{\eta^2}{2} + \frac{P - P_-}{A_0^{4/3} X^{2/3}} + \frac{P'(0-)X^{1/3}\eta}{3A_0^{4/3}} \left\{ \frac{\eta^2}{2} + \frac{P - P_-}{A_0^{4/3} X^{2/3}} [\ln X + 3 \ln \eta + O(1)] \right\}. \quad (\text{A3})$$

For it is the HRW where the inertia terms in (2.14a) are fully restored, the Z -independent contribution to Ψ in (A2) is again in agreement with (2.14c). Thus, matching the X -independent terms in (A1) and (A3) confirms that $f_{\text{HR}} - \eta^2/2 \sim p_{\text{HR}} + \text{TST}$ ($\eta \rightarrow \infty$); matching the higher-order terms achieves the successive emergence of the logarithmic terms.

To this end, we substitute (A1) into (2.14a)–(2.14c) and exploit (A3) with $\eta \gg 1$ kept fixed. This reveals two inhomogeneous linear problems governing F_i ($i = 1, 2$):

$$f'_{\text{HR}} F'_i - f''_{\text{HR}} F_i - 2f_{\text{HR}} F''_i/3 = F'''_i - G_i(\eta), \quad F_i(0) = F''_i(0) = 0, \quad (\text{A4a})$$

$$G_1 := 1, \quad G_2 := 1 + c_2/c_1 + f'_{\text{HR}} F'_1 - f''_{\text{HR}} F_1. \quad (\text{A4b})$$

The well-known behaviour of f_{HR} entails

$$F_1 \sim \gamma_1(\eta^3 + 6p_{\text{HR}}\eta \ln \eta) + \delta_1\eta - 6\gamma_1 + G_1 + O(\eta^{-1}) \quad (\eta \rightarrow \infty) \quad (\text{A5})$$

with some constants γ_1, δ_1 . This is confirmed by expanding (A3) up to $O(X^{1/3} \ln X)$ provided that $\gamma_1 = 0$ and $c_1 = p_{\text{HR}} P'(0-)/(3\delta_1)$. Then $F''_1(\infty) = 0$, and (A4) has a unique non-trivial solution in the case $i = 1$. The numerical method and discretisation we used to compute f_{HR} gives $\delta_1 \simeq -2.6110$, implying $c_1 > 0$. (We also note that $F'_1(0) \simeq -1.8422$.) In turn, $G_2 = 1 + c_2/c_1 + \text{TST}$ ($\eta \rightarrow \infty$) so that (A5) holds also for the corresponding quantities having the subscript 2. Accordingly, expanding (A3) up to $O(X^{1/3})$ then gives $\gamma_2 = P'(0-)/(6c_1) = \delta_1/(2p_{\text{HR}})$. This fixes the missing BC as $F''_2 \sim 3\delta_1\eta/p_{\text{HR}}$ ($\eta \rightarrow \infty$). Adjusting $F'_2(0)$, however, allows this condition to be satisfied for any c_2 as this determined by proceeding in this manner and considering the abbreviated remainder terms in (A1) and (A3).

Appendix B. Outer Rayleigh problem: wavenumber space

We investigate the Rayleigh problem (3.22) in the distinguished limit $T \rightarrow 1-$ and $k \rightarrow 0$, for $|\text{Re } k| \rightarrow \infty$ and the eigenspace (poles) of \mathcal{V} in sufficient detail.

B.1. Singular limits $k \rightarrow 0, T \rightarrow 1-$

The analysis of the long-wave limit $k \rightarrow 0$ is closely related to the discussion of (3.15) with (3.16). We substitute the expansion $\mathcal{V} \sim \sum_{i=0}^{\infty} \kappa_i(k) \mathcal{V}_i(y)$ ($\kappa_{i+1}/\kappa_i \rightarrow 0$) with first unknown gauge functions κ_i and $O(1)$ -functions \mathcal{V}_i into (3.22). In leading order, the problem (3.22) then only permits the homogeneous solution parametrised by κ_0 , thus $\mathcal{V}_0 = \psi'_0$. To allow for deviations from this, the analysis of \mathcal{V}_1 requires $\kappa_1 = O(k^2\kappa_0)$. Specifying $\kappa_1 := k^2\kappa_0$ yields the inhomogeneous problem

$$\mathcal{V}''_1 - (\psi'''_0/\psi'_0)\mathcal{V}_1 = \psi'_0, \quad \mathcal{V}_1(0) = -\kappa_1^{-1}, \quad u_0^+ \mathcal{V}'_1(h_0) = TJ, \quad (\text{B1})$$

where we have anticipated that $\kappa_1 = O(1)$, including the alternative $\kappa_1 \rightarrow \infty$ as $k \rightarrow 0$ as a limiting case. By using the first BC here and after some rearrangements,

$$\frac{\mathcal{V}_1(y)}{\psi'_0(y)} = \alpha_1 - \lambda \kappa_1^{-1} \int_y^{h_0} \frac{dt}{\psi_0'^2(t)} + \int_0^y \frac{dt}{\psi_0'^2(t)} \int_0^t \psi_0'^2(s) ds. \quad (\text{B2})$$

The initially arbitrary constant α_1 indicates again a homogeneous solution and the first BC in (B1) is met in the limit $y \rightarrow 0$. The second BC in (B1) represents a solvability condition for (B1) as it gives

$$\lambda \kappa_1^{-1} = (T - 1)J \quad (\text{B3})$$

to fix $\kappa_0 = \kappa_1/k^2$ with $\kappa_1 = \lambda/[(T - 1)J]$.

This analysis reveals a double pole in $k = 0$ of \mathcal{V} the strength of which increases as $T \rightarrow 1$ above all bounds. It refers to an apparent solution $|\bar{X}|\psi'_0(y)$ ($\bar{X} \neq 0$) to the homogeneous problem formed by (3.14a,c). Since k^2 enters (3.22) linearly, the above expansion is now specified as

$$\mathcal{V} \sim \kappa_0(k) \sum_{i=0}^{\infty} k^{2i} \mathcal{V}_i(y), \quad \mathcal{V}_0 = \psi'_0. \quad (\text{B4})$$

and breaks down passively where $y = O(k^2)$. We solve the arising hierarchy of the inhomogeneous problems

$$\mathcal{V}_i'' - (\psi_0'''/\psi_0')\mathcal{V}_i = \mathcal{V}_{i-1}, \quad \mathcal{V}_i(0) = 0, \quad u_0^{+2} \mathcal{V}_i'(h_0) = T J \mathcal{V}_{i-1}(h_0) \quad (i > 1) \quad (\text{B5})$$

in the fashion achieving (B2):

$$\frac{\mathcal{V}_i(y)}{\psi_0'(y)} = \alpha_i + \int_0^y \frac{dt}{\psi_0'^2(t)} \int_0^t \psi_0'(s) \mathcal{V}_{i-1}(s) ds \quad (\text{B6})$$

where the last BC in (B5) fixes the constant α_{i-1} as function of T in terms of a solvability condition for the problem governing \mathcal{V}_{i-1} . We finally write this constraint after some conversions as the recursive relationship

$$\frac{\mathcal{V}_i(h_0)}{u_0^+} = \frac{\mathcal{I}_i}{1 - T}, \quad \mathcal{I}_i := \frac{1}{J} \int_0^{h_0} \psi_0'^2(y) dy \int_y^{h_0} \frac{dt}{\psi_0'^2(t)} \int_0^t \psi_0'(s) \mathcal{V}_{i-1}(s) ds. \quad (\text{B7})$$

Also, \mathcal{V}_i ($i > 0$) is inversely proportional to $1 - T$.

Inspection of (3.14) reveals immediately the expansion $\bar{V} \sim \bar{a}_+ \psi'_0(y) - \sum_{i=1}^{\infty} \bar{a}_+^{(2i)} \mathcal{V}_i(y)$ ($\bar{X} \rightarrow \infty$) completing (3.15) subject to (3.16) as the reciprocal form to (B4). From this one infers that $\bar{b}_+ = -\alpha_1$.

The above analysis ceases to be valid already when $1 - T$ is so small that $\kappa_1^{-1} = O(k^2)$ and thus no longer enters (B1) but the problem governing \mathcal{V}_2 . However, the asymptotic series (B4) captures this shift of the lower BC formally when we introduce the (positive) parameter

$$\mathcal{T} := (1 - T)/k^2 = O(1) \quad (\text{B8})$$

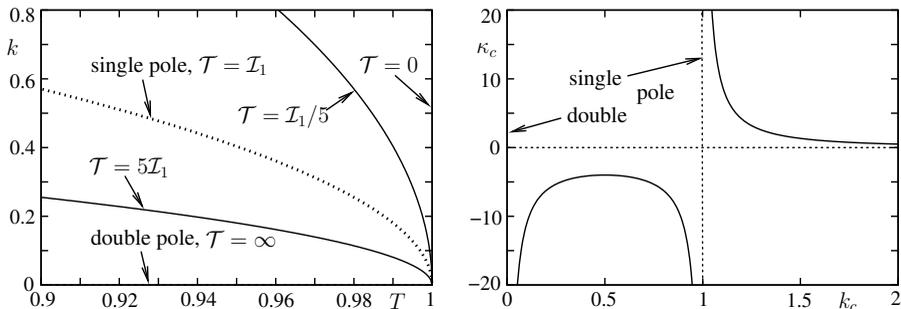
to quantify the consequent least-degenerate distinguished limit. Then κ_1^{-1} is replaced by 0 and T by 1 in (B1), (B2) such that (B3) is satisfied identically. Most importantly, the BCs in (B5) are modified as

$$\mathcal{V}_2(0) = -\kappa_2^{-1}, \quad \mathcal{V}_i(0) = 0 \quad (i > 2), \quad u_0^{+2} \mathcal{V}_i'(h_0) = J[\mathcal{V}_{i-1} - \mathcal{T} \mathcal{V}_{i-2}](h_0) \quad (i > 1) \quad (\text{B9})$$

where we take $\kappa_2 = k^4 \kappa_0$ as of $O(1)$. Hence,

$$\frac{\mathcal{V}_2(y)}{\psi_0'(y)} = \alpha_2 - \lambda \kappa_2^{-1} \int_y^{h_0} \frac{dt}{\psi_0'^2(t)} + \int_0^y \frac{dt}{\psi_0'^2(t)} \int_0^t \psi_0'(s) \mathcal{V}_1(s) ds. \quad (\text{B10})$$

The special form of the dynamic BC in (B9) enforces the determination of the constant α_{i-2} for $i > 2$. It is sufficient for our purposes to concentrate on this BC for $i = 2$. As \mathcal{V}_1 is given by (B6) for $i = 1$, this solvability condition for (B10) yields with the denotation of \mathcal{V}_0 in (B4) and the definitions of \mathcal{I}_1 in (B7) and \mathcal{T} in (B8) after some rearrangements


 FIGURE 12. Plots of poles and variation of \mathcal{V} near $k = 0$, $T = 1$.

an expression for κ_2 and thus κ_0 , independent of the value of α_1 :

$$J\kappa_0/\lambda = k^{-2}[k^2\mathcal{I}_1 - (1 - T)]^{-1}. \quad (\text{B } 11)$$

We find that the distinguished limit (B 8) is rich enough to disclose the behaviour of \mathcal{V} near the critical point $k = 0$ and $T = 1$ (the last case is sorted out here). First, one readily finds that \mathcal{V} admits a regular expansion in $T - 1$ as $T \rightarrow 1$ for $k \neq 0$ or $\mathcal{T} \rightarrow 0$. It is seen that \mathcal{V} attains a fourth-order pole in $k = 0$, $T = 1$ which morphs into a double pole for $T < 1$, here recovered in the limit $\mathcal{T} \rightarrow \infty$ where the two forms of (B 4) considered match. This behavior is associated with the bifurcation of a single pole for k becoming positive, whose location we trace in the (T, k) -plane as

$$k = k_u(T), \quad (\text{B } 12)$$

indicating the existence of undamped capillary oscillations, where $\mathcal{T} \sim \mathcal{I}_1$ or

$$T \sim 1 - \mathcal{I}_1 k_u^2 + O(k_u^4) \quad (k_u \rightarrow 0). \quad (\text{B } 13)$$

As suggested by these asymptotic findings, our numerical study predicts exactly one value of $k^2 = k_u^2$ for each value of T in the relevant interval $0 < T < 1$. We also infer from $\mathcal{V} \sim \text{Res}_{k=k_u}(\mathcal{V})/(k - k_u)$ ($k \rightarrow k_u$), (B 4), (B 11) and (B 13) that

$$\text{Res}_{k=k_u}(\mathcal{V})/\psi'_0(y) \sim \lambda/(2J\mathcal{I}_1 k_u^3) \sim \lambda\mathcal{I}_1^{1/2}/[2J(1 - T)^{3/2}] \quad (k_u \rightarrow 0). \quad (\text{B } 14)$$

The amplitude \bar{a}_u , see (3.25), varies predominantly with $k_u^{-14/3}$ or $(1 - T)^{-7/3}$ in this limit. To exploit the above results numerically, we specify ψ'_0 by Watson’s flow, using (2.7). Then \mathcal{I}_1 can be transformed into a single integral, and we append

$$J = \lambda, \quad \mathcal{I}_1 = \frac{2}{u_0^+} - \frac{1}{\lambda h_0} + \lambda \int_0^{h_0} \left[\frac{1}{\psi_0'^2(y)} - \frac{1}{(\lambda y)^2} \right] dy \simeq 0.307059. \quad (\text{B } 15)$$

The above results can be nicely captured on the basis of (B 8) and (B 11) cast in normal form $\kappa_c = 1/[k_c^2(k_c^2 - 1)]$ employing the canonical variables $k_c := [\mathcal{I}_1/(1 - T)]^{1/2}k$, $\kappa_c := J(1 - T)^2\kappa_0/(\lambda\mathcal{I}_1)$: see figure 12.

B.2. Singular short-wave limit $|\text{Re } k| \rightarrow \infty$

For $|\text{Re } k| \rightarrow \infty$, \mathcal{V} obviously varies exponentially weakly with k . We first identify a viscous sublayer $\zeta := ky = O(1)$ where we take \mathcal{V} as a function of ζ and k . There (3.22a) and (2.5) give $\partial_\zeta \mathcal{V} - \mathcal{V} \sim \omega \zeta \mathcal{V}/k^3 + O(k^{-6})$. In turn,

$$\mathcal{V} \sim e e^{-\zeta} [1 - \omega(\zeta + \zeta^2)/(4k^3) + O(k^{-6})] + (1 - e) e^\zeta [1 - \omega(\zeta - \zeta^2)/(4k^3) + O(k^{-6})] \quad (\text{B } 16)$$

where e is some function of k satisfying $e(-k) \equiv 1 - e(k)$ as (3.22) enforces symmetry of \mathcal{V} with respect to k . For $y = O(1)$, the exponential variation in (B 16) is morphed into a rapid one, typically captured by a Wentzel–Kramers–Brillouin–Jeffreys (WKBJ) ansatz. Inserting this into (3.22a,c) yields after some manipulations and exploiting that symmetry property intrinsic to (3.22)

$$\frac{\mathcal{V}}{E(k)} \sim e^{-k(y-h_0)} \left[1 - \frac{K_0 - K(y)}{2k} + O(k^{-2}) \right] - e^{k(y-h_0)} \left[1 + \frac{K_0 - K(y)}{2k} + O(k^{-2}) \right], \quad (\text{B 17})$$

skew-symmetric in k . The asymptotic relationship $E(k) \equiv -E(-k)$ follows from matching (B 16) and (B 17) as $e(k)$, and

$$K(y) := \int_y^{h_0} \frac{\psi_0'''(t)}{\psi_0'(t)} dt, \quad K_0 := \frac{2\psi_0'^2(h_0)}{TJ}. \quad (\text{B 18})$$

The last constant of integration ensures that (3.22c) is satisfied with the accuracy specified in (B 17) and (B 16), where the terms varying algebraically with k originate in the vorticity of the base flow.

Expanding K for $y \rightarrow 0$ with the help of (2.5) confirms the match of (B 16) and (B 17), up to contributions of respectively $O(k^{-3})$ and $O(k^{-1})$ in the brackets. This first yields two relationships involving e and E : $e \sim E e^{kh_0} [1 - K_0/(2k) + O(k^{-2})]$, $1 - e \sim -E e^{-kh_0} [1 + K_0/(2k) + O(k^{-2})]$. From these we infer

$$e^{-1} \sim 1 - e^{-2kh_0} \mathcal{A}(-k)/\mathcal{A}(k), \quad E^{-1} \sim e^{kh_0} \mathcal{A}(k) - e^{-kh_0} \mathcal{A}(-k) e^{-kh_0} \quad (\text{B 19})$$

where we abbreviate the algebraic variations with k as

$$\mathcal{A}(k) \sim 1 - K_0/(2k) + O(k^{-2}). \quad (\text{B 20})$$

The first of the relations (B 19) verifies that $\mathcal{V} = O(1)$ in (B 16) and the second the exponential smallness of \mathcal{V} for $y \gg |k|$. From (B 17), there

$$\mathcal{V} \sim e^{\mp ky} [1 - K(y)/(K_0 \mp 2k) + O(k^{-3})] + O(e^{\mp k(2h_0-y)}) \quad (k \rightarrow \pm\infty) \quad (\text{B 21})$$

as long as $E \sim e^{-kh_0}/\mathcal{A}(k)$ or $|\mathcal{A}(k)| \gg |e^{-2kh_0}|$ for $\text{Re } k > 0$ and $E \sim e^{kh_0}/\mathcal{A}(-k)$ or $|\mathcal{A}(-k)| \gg |e^{2kh_0}|$ for $\text{Re } k < 0$.

The approximation (B 21) fails when the above constraints are violated, that is, when both contributions to E^{-1} in (B 19) become of the same order of magnitude. The expression for K_0 in (B 18) and (B 20) herald this possibility when T is so small that $k \sim \pm K_0/2 + O(T)$ or $Tk \sim \pm \psi_0'^2(h_0)/J + O(T^2)$. Moreover, E^{-1} might even change sign then, which reveals the emergence of a real pole of \mathcal{V} that represents the small- T asymptote of (B 12):

$$Tk_u [1 + O(k_u^{-1})] = \psi_0'^2(h_0)/J = \sqrt{3/4\pi} \Gamma(\frac{1}{3})/\Gamma(\frac{5}{6}) \simeq 1.15960 \quad (k_u \rightarrow \infty) \quad (\text{B 22})$$

when evaluated for Watson's flow. Since the form of (B 17) depends solely on the homogeneous BC (3.22c), it stays intact then. We also find that $E^{-1} \sim 2(k - k_u) \sinh(k_u h_0)$ when k is arbitrarily close to k_u . Finally, (B 17) yields

$$\text{Res}_{k=k_u}(\mathcal{V}) \sim e^{-k_u h_0} [K(y)/(2k_u) + O(k_u^{-2})] + O(e^{k_u(y-2h_0)}) \quad (k_u \rightarrow \infty). \quad (\text{B 23})$$

These delicate consequences of matching exponentially varying terms advocate a posteriori the inclusion of the algebraically varying ones.

B.3. Eigenspace and poles

As an important aspect, for any $T \geq 0$ the homogeneous version of (3.22) is only solveable only for a countable, infinite set of real eigenvalues of k^2 bounded from above.

When $\bar{\mathcal{V}}_k(y)$ symbolises the space of eigenfunctions,

$$\bar{\mathcal{V}}_k'' = (k^2 + \psi_0'''/\psi_0')\bar{\mathcal{V}}_k, \quad y = 0: \quad \bar{\mathcal{V}}_k = 0, \quad y = h_0: \quad \psi_0'^2\bar{\mathcal{V}}_k' = T J k^2 \bar{\mathcal{V}}_k. \quad (\text{B } 24)$$

In § B.1, we considered the eigenvalue $k = 0$ and the associated double pole. All other eigenvalues are expected to define the single poles of \mathcal{V} in the k -plane: an infinite number of conjugate imaginary and an at most finite number of real ones, these associated with isolated neutral capillary modes. To demonstrate these fundamental properties, we first consider the conjugate-complex of (B 24) and multiply the Rayleigh equation with the complex-conjugate of $\bar{\mathcal{V}}_k$ to obtain the inner product of (B 24) via integration by parts:

$$(k^2 - \bar{k}^2) \left(\frac{TJ}{\psi_0'^2(h_0)} - \int_0^{h_0} |\bar{\mathcal{V}}_k|^2 dy \right) = 0 \quad (\text{B } 25)$$

where \bar{k} is the complex-conjugate of k . That is, (B 24) is not self-adjoint for $T > 0$, and proving that k^2 is indeed real then in standard manner fails. It rather requires transforming (B 24) such that k no longer enters the BC for $y = h_0$. To this end, we introduce the transformed eigenfunctions $\mathcal{F}_k := \psi_0'\bar{\mathcal{V}}_k - \psi_0''\mathcal{V}_k$. We then obtain from (B 24)

$$[\psi_0'^2(\bar{\mathcal{V}}_k/\psi_0')]' \equiv \mathcal{F}_k' = k^2\psi_0'\bar{\mathcal{V}}_k \quad (\text{B } 26)$$

and, since $\psi_0''(h_0) = 0$, $\psi_0'^2\mathcal{F}_k = T J \mathcal{F}_k'$ for $y = h_0$. Differentiation of (B 26) after division by $\psi_0'^2$ casts (B 24) into the form

$$(-\mathcal{F}_k'/\psi_0'^2)' = -k^2\mathcal{F}_k/\psi_0'^2, \quad y = 0: \quad \mathcal{F}_k = 0, \quad y = h_0: \quad \psi_0'^2\mathcal{F}_k = T J \mathcal{F}_k'. \quad (\text{B } 27)$$

Adopting the signs in the usual notation, (B 27) represents a traditional self-adjoint Sturm–Liouville eigenvalue problem with the (for $y \rightarrow 0$ singular) weight function $\psi_0'^{-2}$ for the eigenvalues of $-k^2$. According to classical findings, these indeed form a discrete set $k^2 = k_i^2(T)$ ($i = 0, 1, \dots$) bounded from below and satisfying the Weyl asymptotics $-k_i^2 \sim (\pi i/h_0)^2 + O(i)$ ($i \rightarrow \infty$), controlled by the right-side of the BC for $y = h_0$ (cf. Teschl 2012). Here $k_0^2 = k_u^2 > 0$, referring to the single neutral mode considered in § B.2, so that k_i^2 is set to $-\mu_i^2(T) < 0$ for $i > 0$. It is also noteworthy that this sequence μ_i does not collapse in the limiting case $T = 1$ as $\mu_1(1) \simeq 0.015569$.

Appendix C. Outer Rayleigh problem: diffusive overlayer

Let us take ψ , p , h_+ as functions of \bar{X} , ξ , ϵ . We rectify the Maclaurin expansion of ψ and p for $\xi = O(1)$ justified by (2.3c), (3.10), (3.11) by adding an $O(\epsilon^{5/3})$ -term (and resultant higher-order corrections) that involves the $O(1)$ -functions Ψ^* , P^* so as to account for (2.3d):

$$[\psi, p] \sim [1, P_0(\bar{X})] + \sum_{i=1}^{\infty} [\Psi_i, P_i](\bar{X}; \epsilon) \epsilon^{i/2} \xi^i / i! + \epsilon^{5/3} [\Psi^*, P^*](\bar{X}, \xi) + O(\epsilon^{12/7}). \quad (\text{C } 1)$$

We structure of (C 1) is explained in the following.

The (for $\epsilon \rightarrow 0$) bounded coefficient functions Ψ_i , P_i ($i \geq 0$) ensue from expanding (3.10), (3.11) together with (2.6) and the resultant property $\psi_0''''(h_0) = 0$ (see SBP18). One obtains

$$\Psi_1 \sim u_0^+ + \epsilon^{4/7} m[\psi_* - m\psi_0''''(h_0)A^2(0)/2] + \epsilon^{2/3} \bar{\Psi}_y(\bar{X}, h_0) + O(\epsilon^{5/7}), \quad (\text{C } 2a)$$

$$\Psi_2 \sim \epsilon^{4/7} m[\psi_*'' - \psi_*\psi_0''''/u_0^+](h_0) + \epsilon^{2/3} [\bar{\psi}_{yy}(\bar{X}, h_0) + \bar{H}\psi_0''''(h_0)] + O(\epsilon^{5/7}), \quad (\text{C } 2b)$$

$$[P_0', P_1'] \sim \epsilon^{2/3} [\bar{P}_{\bar{X}}, \bar{P}_{y\bar{X}}](\bar{X}, h_0) + O(\epsilon^{5/7}), \quad P_{1,2} = O(\epsilon^{4/7}), \quad h_{+, \bar{X}} = O(\epsilon^{3/7}). \quad (\text{C } 2c)$$

Substituting (C1) into the shear-layer approximation of (2.3a),

$$\psi_\xi \psi_{\xi \bar{X}} - \psi_{\bar{X}} \psi_{\xi \xi} \sim -\epsilon p_{\bar{X}} - \epsilon^{1/2} h_{+, \bar{X}} p_\xi + \epsilon^{1/2} \psi_{\xi \xi \xi} \quad (\text{C3})$$

(the arising Prandtl shift preserves the convective operator), and collecting powers of ξ yields a hierarchy of relations involving Ψ_i and P_i . Insertion of (C2) into the first two,

$$\Psi_1 \Psi_{1, \bar{X}} \sim -P_{0, \bar{X}} - h_{+, \bar{X}} P_1 - \epsilon \Psi_3, \quad \Psi_1 \Psi_{2, \bar{X}} \sim -P'_1 - h_{+, \bar{X}} P_2 - \epsilon \Psi_4, \quad (\text{C4})$$

just confirms the two-terms expansion of the streamwise momentum equation in (3.12) for $\xi = O(1)$. On the other hand, the left-hand side of (2.3d) reduces to $\Psi_2 - u_0^+ h_{+, \bar{X} \bar{X}} + O(\epsilon^{23/21})$ within the accuracy provided by (3.10), (3.11) and (C2). Evaluating (2.3d) by using (C2b) and (3.10) shows that this BC is satisfied up to $O(\epsilon^{4/7})$ once $m[\psi_*'' - \psi_* \psi_0''' / u_0^+](h_0) + ml^2 u_0^+(G - P_-) = 0$. This constraint for ψ_* must already be provided by the surrounding shear layer addressed in SBP18. However, the follow-up contributions of $O(\epsilon^{2/3})$ to (2.3d) yield in connection with (3.14c) the residual $(\bar{\Psi}_{yy} - \bar{\Psi}_{\bar{X}\bar{X}})(\bar{X}, h_0)$. Compensating this requires indeed the perturbation stream function Ψ^* to enter (C1) at the same order of approximation as the $O(\epsilon^{2/3})$ -contribution to P_2 . In turn, (C3) subject to (2.3c) and (2.3d) yields with the aid of (C2) the diffusion problem

$$u_0^+ \Psi_{\xi \bar{X}}^* = \Psi_{\xi \xi}^*, \quad \xi = 0: \quad \Psi^* = 0, \quad \Psi_{\xi \xi}^* = \bar{\Psi}_{\bar{X}\bar{X}} - \bar{\Psi}_{yy}, \quad \xi \rightarrow -\infty: \quad \Psi_{\xi \xi}^* \rightarrow 0. \quad (\text{C5})$$

This also implies a for $\xi \rightarrow -\infty$ vanishing velocity perturbation Ψ_ξ^* but finite viscous displacement exerted in the bulk flow, measured by $\Psi^*(\bar{X}, \infty)$. The far-upstream and far-downstream asymptotes of Ψ^* are found to be forced by the inhomogeneous BC. Therefore, Ψ^* dies out exponentially for $\bar{X} \rightarrow -\infty$ and grows algebraically for $\bar{X} \rightarrow \infty$. We then use (3.13), (3.15) and (3.16) to describe the merge with the original overlayer (see SBP18) in this limit by $\Psi^* \sim 27\lambda \psi_0'''(h_0) / (80M u_0^+) \bar{X}^{11/3} F_*(\eta_*) + O(\bar{X}^{5/3})$. Herein, the typical Rayleigh variable $\eta_* := \xi \sqrt{u_0^+ / \bar{X}}$ is of $O(1)$ as F_* satisfies

$$19F_*' / 6 - \eta_* F_*'' / 2 = F_*''', \quad F_*(0) = 0, \quad F_*''(0) = 1, \quad F_*''(-\infty) = 0. \quad (\text{C6})$$

The solution to this problem can be expressed in terms of Kummer's confluent hypergeometric function, M :

$$F_*(\eta_*) = (3/11)[M(-\frac{11}{3}, \frac{1}{2}, -\eta_*^2/4) - 1] - \eta_* M(-\frac{19}{6}, \frac{3}{2}, -\eta_*^2/4) / \Gamma(\frac{25}{6}). \quad (\text{C7})$$

Far downstream, the viscous displacement is quantified by $F_*(-\infty) = -3/11$. Adopting the results of §3.3.2, one advantageously expresses the full solution to (C5) as the Fourier integral

$$\Psi^* = \int_{\mathcal{C}} \frac{[k^2 \mathcal{V} + \mathcal{V}_{yy}](k, h_0)}{u_0^+ k^2} \left(1 - e^{\sqrt{i u_0^+} k \xi}\right) e^{ik \bar{X}} dk. \quad (\text{C8})$$

A final remark on the higher-order corrections in (C1) shall advocate self-consistency of the above flow description. The kinematic BC (2.3c) induces an $O(\epsilon^{5/3})$ -disturbance in the expansions of h^+ in (3.10) and thus the capillary pressure jump in (2.3d) such one in (3.11). This produces the non-zero P^* in (C1). In addition, (2.3b) gives $P_\xi^* \equiv 0$.

Appendix D. Extended Jeffrey–Hamel limit

We address briefly two formal aspects of the JH limit.

At first, inspection of (4.4) suggests the local expansion

$$\bar{\psi} \sim \bar{g}(\vartheta) + \bar{r}^\sigma G(\vartheta) + o(\bar{r}^\sigma) + c.c., \quad \text{Re } \sigma > 0. \quad (\text{D1})$$

Here σ denotes the eigenvalue and G the corresponding eigenfunction satisfying the resulting eigenvalue problem

$$\begin{aligned} & [\sigma^2(\sigma - 2)\bar{g}' - \sigma\bar{g}''']G - 2\bar{g}''G' + (\sigma - 2)\bar{g}'G'' = \\ & [(\sigma - 2)^2 + d^2/d\vartheta^2](\sigma^2G + G''), \end{aligned} \quad (\text{D } 2a)$$

$$G(0) = G'(0) = G(\pi) = G'(\pi) = 0. \quad (\text{D } 2b)$$

In (D 1), σ then specifies the instance in the discrete series of eigenvalues having minimum positive real part. The validity of the JH solution and thus the local representation (D 1) of the full NS solution depends on the existence of this instance.

Secondly, we envisage \bar{p} and \bar{h} , related via the dynamic BC in (4.3c), near $\bar{r} = 0$. The pressure gradient ensues from the momentum equations (4.3a,b) in the form $\bar{p}_{\bar{r}} \sim (\bar{g}''' + \bar{g}'^2)/\bar{r}^3 = [\bar{g}'''(\pi) - 4\bar{g}']/\bar{r}^3$, where the last equality follows from (4.6) upon integration, and $\bar{p}_{\vartheta} \sim 2\bar{g}''/\bar{r}^2$. Finally,

$$\bar{p} \sim [4\bar{g}' - \bar{g}'''(\pi)]/(2\bar{r}^2) + o(\bar{r}^{-2}) \quad (\bar{r} \rightarrow 0), \quad \bar{h} \sim \bar{g}'''(\pi) \ln \bar{x}/(2\tau) \quad (\bar{x} \rightarrow 0+) \quad (\text{D } 3)$$

with $g'''(\pi) \simeq 87.9545$ ($\bar{g}'''(\pi) \simeq 19.6983$) for the attached (detached) eddy and for any finite value of τ . These singularities are much stronger than those found for the alternative Stokes limit (§ 4.2.2). Accordingly, their resolution would take place in further NS region defined by the smallest scales, describing the microscopic resolution of the trailing edge.

Appendix E. Eigensolutions of the Stokes operator having weakly non-algebraic radial variation?

Given the absence of a reference length and velocity of the Stokes limit considered, typical dimensional reasoning predicts, in general, algebraic–logarithmic variations of the gauge functions in (4.8) with \bar{r} . Nonetheless, the following analysis confirms that factors with sub-algebraic (logarithmic) dependence on \bar{r} do not contribute to (4.8).

Seeking eigensolutions of the biharmonic operator in the limit $\bar{r} \rightarrow 0$ first leaves one with a generalisation of the expansion into eigenfunction in (4.8):

$$\psi \sim \sum_{i=j=0}^{\infty} \bar{r}^{\sigma_i} \chi_{i,j}(\bar{r}) f_{i,j}(\vartheta), \quad \chi_{i,j+1} = o(\chi_{i,j}). \quad (\text{E } 1)$$

Herein, $f_{i,j}$ indicates the double series of eigenfunctions, with $f_{i,0} = f_i$ as we found so far, due to the corresponding sought gauge functions $\chi_{i,j}$ exhibiting sub-algebraic variation, including the previous situation $\chi_{i,0} \equiv 1$ and $f_{i,j} \equiv \chi_{i,j} \equiv 0$ for $j > 0$. Following the analysis of Scheichl (2014) of the Laplace operator, for any such function $\Xi_{i,j} := \bar{r}\chi'_{i,j}$ is of $o(\chi_{i,j})$ and again belongs to this family of functions. With this relation in mind, we obtain after some rearrangements

$$\bar{\Delta}^2(\bar{r}^{\sigma_i} \chi_{i,j} f_{i,j}) \sim \Xi_{i,j} J_{i,j}(\vartheta) + o(\Xi_{i,j}), \quad J_{i,j}(\vartheta) := 4(\sigma_i - 1)[f''_{i,j} + \sigma_i(\sigma_i - 2)f_{i,j}] \quad (\text{E } 2)$$

(agreeing with the symmetry of $f_{i,j}$ in σ_i with respect to $\sigma_i = 1$). In turn, we specify $\chi_{i,1} = -\Xi_{i,0}$. If $\chi_{i,1}$ does not vanish identically, the homogeneous problem determining f_i yields the inhomogeneous follow-up problem fixing $f_{i,1}$ according to (4.9)

$$\mathcal{S}_i\{f_{i,1}\} = J_{i,0}(\vartheta), \quad f_{i,1}(0) = f''_{i,1}(0) = f_{i,1}(\pi) = f'_{i,1}(\pi) = 0. \quad (\text{E } 3)$$

Since the homogeneous operator in (E 3) and defined by (4.9) is self-adjoint,

$$0 = \int_0^\pi \mathcal{S}_i\{f_{i,1}\} f_i(\vartheta) \, d\vartheta = \int_0^\pi J_{i,0}(\vartheta) f_i(\vartheta) \, d\vartheta = 8\pi(-1)^i (\sigma_i - 1) a_i b_i \quad (\text{E } 4)$$

with the aid of (4.10). This contradiction implies $\chi_{i,0} \equiv 1$, $\chi_{i,1} \equiv 0$ and, by iteration, $\chi_{i,j} \equiv 0$ for all $j > 0$. Consequently, the appearance of sub-algebraic factors in (4.8) is indeed ruled out.

REFERENCES

- BONN, D., EGGERS, J., INDEKEU, J., MEUNIER, J. & ROLLEY, E. 2009 Wetting and spreading. *Rev. Mod. Phys.* **81** (2), 739–805.
- BOWLES, R. I. & SMITH, F. T. 1992 The standing hydraulic jump: theory, computations and comparisons with experiments. *J. Fluid Mech.* **242**, 145–168.
- CUMBERBATCH, E. & NORBURY, J. 1979 Capillary modification of the singularity at a free-streamline separation point. *Q. J. Mech. Appl. Math.* **32** (3), 303–312.
- DEPRIMA, C. R. & WU, T. Y. 1957 On the theory of surface waves generated by moving disturbances. *Calif. Inst. Tech. Eng. Div. Rept.* 21–23.
- DRAZIN, P. G. & REID, W. H. 2004 *Hydrodynamic Stability*, 2nd ed., Cambridge Mathematical Library. Cambridge University Press.
- DUEZ, C., YBERT, CH., CLANET, CH. & BOCQUET, L. 2010 Wetting controls separation of inertial flows from solid surfaces. *Phys. Rev. Lett.* **8** (4), 084503–1–084504–4 (doi.org/10.1103/PhysRevLett.104.084503).
- DYSON, D. C. 1988 Contact line stability at edges: Comments on Gibb’s inequalities. *Phys. Fluids* **31** (2), 229–232.
- FRAENKEL, L. E. 1962 Laminar flow in symmetrical channels with slightly curved walls, I. On the Jeffery–Hamel solutions for flow between plane walls. *Proc. R. Soc. Lond. A* **267** (1328), 119–138.
- GAJJAR, J. S. B. 1987 Fully developed free surface flows—Liquid layer flow over a convex corner. *Comput. Fluids* **15** (4), 337–360.
- GOLDSTEIN, S. 1930 Concerning some solutions of the boundary layer equations in hydrodynamics. *Math. Proc. Cambridge* **26** (1), 1–30.
- HAKKINEN, R. J. & ROTT, N. 1965 Similar solutions for merging shear flows II (Technical Note). *AIAA J.* **3** (8), 1553–1554.
- HIGUERA, F. J. 1994 The hydraulic jump in a viscous laminar flow. *J. Fluid Mech.* **274**, 69–92.
- HUERRE, P. & MONKEWITZ, P. A. 1990 Local and global instabilities in spatially developing flows. *Ann. Rev. Fluid Mech.* **22**, 473–537.
- JAMBON-PUILLET, E., BOUWHUIS, W., SNOELJDER, J. H. & BONN, D. 2019 Liquid helix: how capillary jets adhere to vertical cylinders. *Phys. Rev. Lett.* **122** (18), 184501–1–184501–5.
- KELLER, J. B. 1957 Teapot effect. *J. Appl. Phys.* **28** (8), 859–864.
- KISTLER, S. F. & SCRIVEN, L. E. 1994 The teapot effect: sheet-forming flows with deflection, wetting and hysteresis. *J. Fluid Mech.* **263**, 19–62.
- KLUWICK, A., COX, E. A., EXNER, A. & GRINSCHGL, CH. 2010 On the internal structure of weakly nonlinear bores in laminar high Reynolds number flow. *Acta Mech.* **210** (1–2), 135–157.
- MESSITER, A. F. 1970 Boundary-layer flow near the trailing edge of a flat plate. *SIAM J. Appl. Math.* **18** (1), 241–257.
- MOFFATT, H. K. 1964 Viscous and resistive eddies near a sharp corner. *J. Fluid Mech.* **18** (1), 1–18.
- OLIVER, J. F., HUH, C. & MASON, S. G. 1977 Resistance to spreading of liquids b sharp edges. *J. Colloid Interf. Sci.* **59** (3), 568–581.
- REINER, M. 1956 The teapot effect ... a problem. *Phys. Today* **9**(9), 16–20.
- SCHEICHL, B. 2014 A note on the far-asymptotics of Helmholtz–Kirchhoff flows. *Theor. Comput. Fluid Dyn.* **28** (3), 377–384.
- SCHEICHL, B., BOWLES, R. I. & PASIYAS, G. 2018 Developed liquid film passing a trailing edge under the action of gravity and capillarity. *J. Fluid Mech.* **850**, 924–953.
- SCHEICHL, B., BOWLES, R. I. & PASIYAS, G. 2019 Choking and hydraulic jumps in laminar flow. *Proc. Appl. Maths Mech.* **19** (1), e201900489663 (2 p.).
- SCHEICHL, B. & KLUWICK, A. 2019 Laminar spread of a circular liquid jet impinging axially on a rotating disc. *J. Fluid Mech.* **864**, 449–489.

- SMITH, F. T. 1977 Upstream interactions in channel flows. *J. Fluid Mech.* **79** (4), 631–655.
- SMITH, F. T. 1978 A note on a wall jet negotiating a trailing edge. *Q. J. Mech. Appl. Maths* **31** (4), 473–479.
- SMITH, F. T. & DUCK, P. W. 1977 Separation of jets or thermal boundary layers from a wall. *Q. J. Mech. Appl. Maths* **30** (2), 143–156.
- STEWARTSON, K. 1968 On the flow near the trailing edge of a flat plate. *Proc. R. Soc. Lond. A* **306** (1486), 275–290.
- STEWARTSON, K. 1969 On the flow near the trailing edge of a flat plate II. *Mathematika* **16** (1), 106–121.
- TELETZKE, G. F., DAVIES, H. T. & SCRIVEN, L. E. 1988 Wetting hydrodynamics. *Rev. Phys. Appl.* **23** (6), 989–1007.
- TESCHL, G. 2012 *Ordinary Differential Equations and Dynamical Systems*, Graduate Studies in Mathematics, vol. 140. AMS.
- THE MATHWORK INC. 2020 MATLAB. *version 9.9 (R2020b)*. Natick, MA (uk.mathworks.com).
- THE NUMERICAL ALGORITHMS GROUP (NAG) 2020 The NAG Toolbox for MATLAB®. Oxford, UK (www.nag.com).
- TILLET, J. P. K. 1968 On the laminar flow in a free jet of liquid at high Reynolds numbers. *J. Fluid Mech.* **32** (2), 273–292.
- VANDEN-BROECK, J.-M. & KELLER, J. B. 1986 Pouring flows. *Phys. Fluids* **29** (12), 3958–3961.
- VANDEN-BROECK, J.-M. & KELLER, J. B. 1989 Pouring flows with separation. *Phys. Fluids A* **1** (1), 156–158.
- VANDEN-BROECK, J.-M. 2010 *Gravity–Capillary Free-Surface Flows*, Cambridge Monographs on Mechanics. Cambridge University Press.
- WATSON, E. J. 1964 The radial spread of a liquid jet over a horizontal plane. *J. Fluid Mech.* **20** (3), 481–499.
- WHYMAN, G., BORMASHENKO, E. & STEIN, T. 2008 The rigorous derivation of Young, Cassie–Baxter and Wenzel equations and the analysis of the contact angle hysteresis phenomenon. *Chem. Phys. Lett.* **450** (4), 355–359.
- YAPALPARVI, R. 2012 Double-deck structure revisited. *Eur. J. Mech. B-Fluid.* **31**, 53–70.